

**AFRL-SN-RS-TR-2005-292**  
**Final Technical Report**  
**August 2005**



# **IMAGING THAT EXPLOITS MULTIPATH SCATTERING**

**Rensselaer Polytechnic Institute**

*APPROVED FOR PUBLIC RELEASE; DISTRIBUTION UNLIMITED.*

**AIR FORCE RESEARCH LABORATORY  
SENSORS DIRECTORATE  
ROME RESEARCH SITE  
ROME, NEW YORK**

## **STINFO FINAL REPORT**

This report has been reviewed by the Air Force Research Laboratory, Information Directorate, Public Affairs Office (IFOIPA) and is releasable to the National Technical Information Service (NTIS). At NTIS it will be releasable to the general public, including foreign nations.

AFRL-SN-RS-TR-2005-292 has been reviewed and is approved for publication

APPROVED:     /s/  
CARL R. THOMAS  
Project Engineer

FOR THE DIRECTOR:     /s/  
RICHARD G. SHAUGHNESSY, Chief  
Rome Operations Office  
Sensors Directorate

<b>REPORT DOCUMENTATION PAGE</b>			Form Approved OMB No. 074-0188	
Public reporting burden for this collection of information is estimated to average 1 hour per response, including the time for reviewing instructions, searching existing data sources, gathering and maintaining the data needed, and completing and reviewing this collection of information. Send comments regarding this burden estimate or any other aspect of this collection of information, including suggestions for reducing this burden to Washington Headquarters Services, Directorate for Information Operations and Reports, 1215 Jefferson Davis Highway, Suite 1204, Arlington, VA 22202-4302, and to the Office of Management and Budget, Paperwork Reduction Project (0704-0188), Washington, DC 20503				
<b>1. AGENCY USE ONLY (Leave blank)</b>		<b>2. REPORT DATE</b> AUGUST 2005	<b>3. REPORT TYPE AND DATES COVERED</b> Final Aug 03 – May 05	
<b>4. TITLE AND SUBTITLE</b> IMAGING THAT EXPLOITS MULTIPATH SCATTERING			<b>5. FUNDING NUMBERS</b> C - F30602-03-1-0230 PE - 62204F PR - 517R TA - 15 WU - 02	
<b>6. AUTHOR(S)</b> Margaret Cheney				
<b>7. PERFORMING ORGANIZATION NAME(S) AND ADDRESS(ES)</b> Rensselaer Polytechnic Institute 110 Eight Street Troy New York 12180-3590			<b>8. PERFORMING ORGANIZATION REPORT NUMBER</b>  N/A	
<b>9. SPONSORING / MONITORING AGENCY NAME(S) AND ADDRESS(ES)</b> Air Force Research Laboratory/SNRT 26 Electronic Parkway Rome New York 13441-4514			<b>10. SPONSORING / MONITORING AGENCY REPORT NUMBER</b>  AFRL-SN-RS-TR-2005-292	
<b>11. SUPPLEMENTARY NOTES</b>  AFRL Project Engineer: Carl R. Thomas/SNRT/(315) 330-2600/ Carl.Thomas@rl.af.mil				
<b>12a. DISTRIBUTION / AVAILABILITY STATEMENT</b> APPROVED FOR PUBLIC RELEASE; DISTRIBUTION UNLIMITED.				<b>12b. DISTRIBUTION CODE</b>
<b>13. ABSTRACT (Maximum 200 Words)</b> Work has focused on three radar imaging problems: a) analysis of different measurement scenarios for imaging within a parallel-plate waveguide (a simple model for an urban setting), b) imaging from high-doppler-resolution radar data, and c) imaging that exploits multipath scattering.				
<b>14. SUBJECT TERMS</b> Imaging, Multipath Scattering, Urban				<b>15. NUMBER OF PAGES</b> 63
				<b>16. PRICE CODE</b>
<b>17. SECURITY CLASSIFICATION OF REPORT</b>  UNCLASSIFIED	<b>18. SECURITY CLASSIFICATION OF THIS PAGE</b>  UNCLASSIFIED	<b>19. SECURITY CLASSIFICATION OF ABSTRACT</b>  UNCLASSIFIED	<b>20. LIMITATION OF ABSTRACT</b>  UL	

# Table of Contents

<b>1</b>	<b>Imaging in a parallel-plate waveguide</b>	<b>1</b>
1.1	Basic theory . . . . .	1
1.1.1	Model for wave propagation in free space . . . . .	1
1.1.2	Wave propagation in the waveguide . . . . .	2
1.1.3	The model for scattering from the target . . . . .	3
1.1.4	Arrays of sources . . . . .	4
1.2	Monostatic imaging . . . . .	5
1.3	Bistatic imaging . . . . .	5
<b>2</b>	<b>Imaging from high-Doppler-resolution waveforms</b>	<b>6</b>
2.1	Introduction . . . . .	6
2.2	Radar data . . . . .	8
2.2.1	The scattered field . . . . .	8
2.2.2	Correlation data . . . . .	9
2.3	The Case of a Straight Flight Path and Flat Earth . . . . .	10
2.3.1	Image formation . . . . .	11
2.3.2	Resolution . . . . .	12

2.3.3	Numerical Implementation . . . . .	14
2.4	Conclusions and Future Work . . . . .	16
<b>3</b>	<b>Imaging that exploits multipath scattering</b>	<b>18</b>
3.1	Introduction . . . . .	18
3.2	The Mathematical model . . . . .	19
3.2.1	A model for the wave propagation . . . . .	19
3.2.2	A model for the antenna . . . . .	21
3.2.3	Multiple scattering from point scatterers . . . . .	21
3.2.4	The model for scattering from the target . . . . .	24
3.3	Image formation . . . . .	24
3.3.1	General strategy . . . . .	25
3.3.2	Case of a single point scatterer . . . . .	25
3.4	Resolution . . . . .	36
3.5	Conclusions from the theoretical study . . . . .	36
3.6	Simulations . . . . .	37
3.6.1	Simulation of single-view data . . . . .	38
3.6.2	Reconstructions from a single view . . . . .	38
3.6.3	Simulation of multiple-view data . . . . .	39
3.6.4	Multiple-view reconstruction . . . . .	40
3.6.5	Work with data from the radar range . . . . .	40
3.6.6	Issues for the future . . . . .	41
	Bibliography.....	54

# List of Figures

1.1	Scattering geometry. The darker walls and dot denote the true walls and a point source; the lighter ones represent virtual walls and corresponding virtual sources. . . . .	1
2.1	A high-range-resolution system. . . . .	6
2.2	A high-Doppler-resolution system. . . . .	7
2.3	The Doppler return from three point scatterers. . . . .	16
2.4	The (resampled) Radon-Hough transform of the data in Figure 3.7. The true locations are marked by $\circ$ ; the light path is along the $z_1$ axis. . . . .	16
3.1	Scattering geometry . . . . .	19
3.2	Region in Fourier space obtained from $K_{1,1}$ . . . . .	36
3.3	Region in Fourier space obtained from $K_{2,2}$ . . . . .	37
3.4	Region in Fourier space obtained from $K_{3,3}$ . . . . .	38
3.5	A time-domain plot of (the magnitude of) data from two point scatterers. The first two peaks are from direct scattering; the third peak is from the wave that bounces off one scatterer onto the second and then propagates back to the radar . . . . .	39
3.6	The single-bounce backprojected image of a point scatterer, with the true locations shown as yellow circles. The radar position is the red cross superimposed on the scale at the bottom. The multipath scattering appears as a second scatterer located farther away from the radar. Note that no cross-range information can be obtained from this single view. . . . .	43

3.7	The double-bounce backprojected image from two point scatterers, with the true locations shown as yellow circles. In this image, the single-bounce scattering causes an artifact. . . . .	44
3.8	The backprojected image from two point scatterers; this is a superposition of Figures 2 and 3. The true locations are shown as yellow circles. See the text for discussion. . . . .	45
3.9	Range-angle plot of multiple-view data for two scatterers. Here views are taken every $.5^\circ$ over angles from 0 to $90^\circ$ . . . . .	46
3.10	Single-bounce reconstruction from 10 views spanning $90^\circ$ (each $9^\circ$ apart). The radar starts from the top and moves to the left side. . . . .	46
3.11	Double-bounce reconstruction from the same dataset as Figure 3.10. . . . .	47
3.12	The sum of Figures 3.10 and 3.11 . . . . .	48
3.13	The red line is a horizontal slice through Figure 3.10 (the single-bounce backprojection); the green line is the same slice through Figure 3.12 (the sum of the single-bounce and double-bounce backprojections). This shows the improvement from adding the double-bounce backprojection. . . . .	49
3.14	Range-angle plot of the (magnitude of) the experimental data from 3 pipes. . . . .	50
3.15	Range-angle plot of the (magnitude of) the experimental data from a single pipe. . . . .	51
3.16	Range-angle plot of the (magnitude of) the experimental data from two pipes. . . . .	52
3.17	The single-bounce backprojected image from the 3-pipe data. The radar moves over $12^\circ$ at the top. . . . .	53

# Chapter 1

## Imaging in a parallel-plate waveguide

This is joint work with Cliff Nolan. Work on this project is still ongoing.

### 1.1 Basic theory

The mathematical model involves a number of ingredients: 1) a model for wave propagation in free space, 2) a model for multiple scattering from buildings, 3) a (linearized) model for scattering from the scene, and 4) a model for the array of sources.

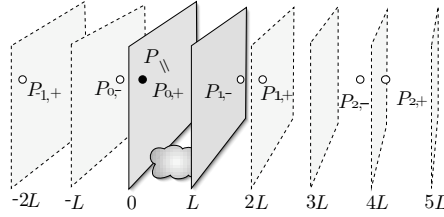


Figure 1.1: Scattering geometry. The darker walls and dot denote the true walls and a point source; the lighter ones represent virtual walls and corresponding virtual sources.

#### 1.1.1 Model for wave propagation in free space

We assume that waves propagate within the waveguide according to the scalar wave equation:

$$\nabla^2 u - c_0^{-2} \ddot{u} = 0, \quad (1.1)$$

where the dots denote differentiation with respect to  $t$  and  $c_0$  is the speed of light.



The eld due to a point source at  $\mathbf{P} = 0$  at time  $t = 0$  is

$$g_0(t, |\mathbf{P}|) = \frac{\delta(t - |\mathbf{P}|/c_0)}{4\pi|\mathbf{P}|} = \int \frac{e^{-i\omega(t-|\mathbf{P}|/c_0)}}{4\pi|\mathbf{P}|} d\omega \quad (1.2)$$

We will use capital letters for frequency-domain quantities, which are related to time-domain quantities by the Fourier transform

$$U(\omega, \mathbf{P}) = \frac{1}{2\pi} \int e^{i\omega t} u(t, \mathbf{P}) dt. \quad (1.3)$$

We write  $k = \omega/c_0$ .

### 1.1.2 Wave propagation in the waveguide

We consider the waveguide formed by two infinite parallel walls. We take one wall to be the plane  $x = 0$  and the other to be the plane  $x = L$ . We assume that on the walls, the electromagnetic eld satisfies the boundary condition

$$\frac{\partial u}{\partial x} = 0 \quad (1.4)$$

Consequently a Green's function for the waveguide can be constructed by the method of images:

$$G(\omega, \mathbf{P}, \mathbf{P}') = \sum_{\alpha \in \{\pm\}} \sum_{n=-\infty}^{\infty} \frac{e^{ik|\mathbf{P}-\mathbf{P}'_{n,\alpha}|}}{4\pi|\mathbf{P}-\mathbf{P}'_{n,\alpha}|} \quad (1.5)$$

where the  $\mathbf{P}'_{n,\pm}$  are the *virtual images* of  $\mathbf{P}'$ : if  $\mathbf{P}' = (x', y', z')$ , then  $\mathbf{P}'_{n,+} = (x' + 2nL, y', z')$  and  $\mathbf{P}'_{n,-} = (-x' + 2nL, y', z')$  (See Fig. 3.1). The sum in (1.5) is over all the virtual images.

We note that the virtual images satisfy certain symmetry relations:

$$\begin{aligned} |\mathbf{P} - \mathbf{P}'_{n,+}| &= \sqrt{[x - (x' + 2nL)]^2 + \dots} = |\mathbf{P}_{-n,+} - \mathbf{P}'| \\ |\mathbf{P} - \mathbf{P}'_{n,-}| &= \sqrt{[x - (-x' + 2nL)]^2 + \dots} \\ &= \sqrt{[-x + 2nL - x']^2 + \dots} = |\mathbf{P}_{n,-} - \mathbf{P}'| \end{aligned} \quad (1.6)$$

and that

$$(\mathbf{P} + \mathbf{p})_{n,\alpha} = \mathbf{P}_{n,\alpha} + \mathbf{p}_{0,\alpha}. \quad (1.7)$$

We use tildes to indicate reflection of the  $x$ -coordinate about the  $y$ - $z$ -plane:  $\tilde{\mathbf{p}} = \mathbf{p}_{0,-}$  and  $\tilde{\tilde{\mathbf{p}}}_{0,-} = \mathbf{p} = \mathbf{p}_{0,+}$ .

Within the region  $-L < x < L$ ,  $G$  satisfies

$$\nabla^2 G(\omega, \mathbf{P}, \mathbf{P}') + k^2 G(\omega, \mathbf{P}, \mathbf{P}') = -\delta(\mathbf{P}, \mathbf{P}') \quad (1.8)$$

To model a finite waveguide, say one extending up to height  $z = H$ , we include only certain of the virtual sources.

### 1.1.3 The model for scattering from the target

We model the target as a change in wave speed  $V(\mathbf{P}) = c^{-2}(\mathbf{P}) - c_0^{-2}$ . The scattered field  $U^{\text{sc}}(\omega, \mathbf{P}, \mathbf{P}')$  at  $\mathbf{P}$  due to an incident field  $U^{\text{in}}(\omega, \mathbf{P}, \mathbf{P}') = G(\omega, \mathbf{P}, \mathbf{P}')$  is given by [31] the Lippmann-Schwinger equation:

$$U^{\text{sc}}(\omega, \mathbf{P}, \mathbf{P}') = \int G(\omega, \mathbf{P}, \mathbf{P}'') \omega^2 V(\mathbf{P}'') [G(\omega, \mathbf{P}'', \mathbf{P}') + U^{\text{sc}}(\omega, \mathbf{P}'', \mathbf{P}')] d\mathbf{P}'' \quad (1.9)$$

We wish to reconstruct  $V$  from knowledge of  $G^{\text{sc}}$ .

Unfortunately (1.9) is an integral equation whose solution  $U^{\text{sc}}$  depends in a nonlinear way on  $V$ . To simplify the problem, we make the *Born* or *single-scattering* approximation: we neglect the term involving  $U^{\text{sc}}$  on the right side of (1.9). This gives us

$$U_B^{\text{sc}}(\omega, \mathbf{P}, \mathbf{P}') = \int G(\omega, \mathbf{P}, \mathbf{P}'') \omega^2 V(\mathbf{P}'') G(\omega, \mathbf{P}'', \mathbf{P}') d\mathbf{P}'' \quad (1.10)$$

The Born approximation makes the mapping from  $V$  to  $U^{\text{sc}}$  linear, but it is not necessarily a good approximation. Another linearizing approximation that can be used for reflection from smooth surfaces is the *Kirchhoff approximation*, in which the scattered field is replaced by its geometrical optics approximation. Here, however, we consider only the Born approximation.

The corresponding time-domain field is

$$u_B^{\text{sc}}(t, \mathbf{P}, \mathbf{P}') = \int e^{-i\omega t} G(\omega, \mathbf{P}, \mathbf{P}'') V(\mathbf{P}'') G(\omega, \mathbf{P}'', \mathbf{P}') \omega^2 d\omega d\mathbf{P}'' \quad (1.11)$$

We note that since  $G$  is given by a sum (1.5), (1.11) is of the form

$$u_B^{\text{sc}}(t, \mathbf{P}, \mathbf{P}') = \sum_{\alpha, \beta \in \{\pm\}} \sum_{m, n} F_{n, \alpha, m, \beta}[V](t, \mathbf{P}, \mathbf{P}') \quad (1.12)$$

where

$$F_{n, \alpha, m, \beta}[V](t, \mathbf{P}, \mathbf{P}') = \int \frac{e^{-i\omega(t - |\mathbf{P} - \mathbf{P}_{n, \alpha}'|/c_0)}}{4\pi |\mathbf{P} - \mathbf{P}_{n, \alpha}'|} V(\mathbf{P}'') \frac{e^{i\omega|\mathbf{P}'' - \mathbf{P}_{m, \beta}'|/c_0}}{4\pi |\mathbf{P}'' - \mathbf{P}_{m, \beta}'|} \omega^2 d\omega d\mathbf{P}'' \quad (1.13)$$

To the initial factors in (1.13) we apply the symmetry relations (1.6) and then we re-label the indices of (1.12) to write  $u^{\text{sc}}$  in the same form (1.12) with

$$F_{n, \alpha, m, \beta}[V](t, \mathbf{P}, \mathbf{P}') = \int \frac{e^{-i\omega(t - |\mathbf{P}_{n, \alpha} - \mathbf{P}''|/c_0)}}{4\pi |\mathbf{P}_{n, \alpha} - \mathbf{P}''|} V(\mathbf{P}'') \frac{e^{i\omega|\mathbf{P}'' - \mathbf{P}_{m, \beta}'|/c_0}}{4\pi |\mathbf{P}'' - \mathbf{P}_{m, \beta}'|} \omega^2 d\omega d\mathbf{P}'' \quad (1.14)$$

### 1.1.4 Arrays of sources

We consider arrays of isotropically-radiating sources. At frequency  $\omega$ , the eld at  $\mathbf{P}''$  emanating from the source at  $\mathbf{P}'$  is  $G(\omega, |\mathbf{P}'' - \mathbf{P}'|)$ , where  $G$  is given by (1.5). To model the eld  $u^{\text{in}}$  from an array, centered at  $\mathbf{P}'$ , in which the element at  $\mathbf{P}' + \mathbf{p}'$  is activated with the waveform  $j(t, \mathbf{p}')$ , we simply integrate:

$$u^{\text{in}}(t, \mathbf{P}'') = \int_{-\infty}^{\infty} e^{-i\omega t} \int_{\text{array}} G(\omega, |\mathbf{P}'' - (\mathbf{P}' + \mathbf{p}')|) J(\omega, \mathbf{p}') d\mathbf{p}' d\omega. \quad (1.15)$$

(Here  $J$  denotes the Fourier transform of  $j$ .)

To obtain the corresponding scattered eld, we apply the same operation to  $u^{\text{sc}}$  (because the mapping from incident eld to scattered eld is linear). We denote the resulting Born-approximated eld by  $u_{j,B}^{\text{sc}}$ :

$$u_{j,B}^{\text{sc}}(t, \mathbf{P}, \mathbf{P}') = \int e^{-i\omega t} G(\omega, \mathbf{P}, \mathbf{P}'') V(\mathbf{P}'') \int_{\text{array}} G(\omega, \mathbf{P}'', \mathbf{P}' + \mathbf{p}') J(\omega, \mathbf{p}') d\mathbf{p}' \omega^2 d\omega \quad (1.16)$$

An array can form a steered beam by including phasing in  $j$ . For example, for a unit vector  $\boldsymbol{\mu}$ , a beam steered in direction  $\boldsymbol{\mu}$  and be produced by taking  $J_{\boldsymbol{\mu}}(\omega, \mathbf{p}') = J(\omega) \exp(ik\boldsymbol{\mu} \cdot \mathbf{p}') \chi_{\text{array}}(\mathbf{p}')$ , where  $\chi_{\text{array}}$  denotes a function that is smooth on the array and zero off it.

We assume that  $\mathbf{p}'$  is small compared to  $|\mathbf{P}'' - \mathbf{P}'|$ , which enables us to use the expansion

$$|\mathbf{P}'' - (\mathbf{P}' + \mathbf{p}')| = |\mathbf{P}'' - \mathbf{P}'| - \widehat{\mathbf{P}'' - \mathbf{P}'} \cdot \mathbf{p}' + \dots \quad (1.17)$$

in the Fourier-transformed version of (1.15):

$$\begin{aligned} U^{\text{in}}(\omega, \mathbf{P}'', \mathbf{P}') &= \sum_{\alpha \in \{\pm\}} \sum_n \int \frac{e^{ik(|\mathbf{P}'' - \mathbf{P}'_{n,\alpha} - \mathbf{p}'_{0,\alpha}|)} J(\omega) e^{-ik\boldsymbol{\mu} \cdot \mathbf{p}'} \chi_{\text{array}}(\mathbf{p}') d\mathbf{p}'}{4\pi |\mathbf{P}'' - \mathbf{P}'_{n,\alpha} - \mathbf{p}'_{0,\alpha}|} \\ &= \sum_{\alpha \in \{\pm\}} \sum_n \int \frac{e^{ik(|\mathbf{P}'' - \mathbf{P}'_{n,\alpha}| - \widehat{\mathbf{P}'' - \mathbf{P}'_{n,\alpha}} \cdot \mathbf{p}'_{0,\alpha} + \dots)} J(\omega) e^{-ik\boldsymbol{\mu} \cdot \mathbf{p}'} \chi_{\text{array}}(\mathbf{p}') d\mathbf{p}'}{4\pi |\mathbf{P}'' - \mathbf{P}'_{n,\alpha}|} \end{aligned} \quad (1.18)$$

Arrays are often planar; in this case the  $\mathbf{p}'$  integration is two-dimensional. For a planar array and  $\alpha = +$ , the integral

$$\int_{\text{array}} e^{-ik(\widehat{\mathbf{P}'' - \mathbf{P}'_{n,\alpha}} \cdot \mathbf{p}'_{0,+} - \boldsymbol{\mu} \cdot \mathbf{p}') d\mathbf{p}'} = \int_{\text{array}} e^{-ik(\widehat{\mathbf{P}'' - \mathbf{P}'_{n,\alpha}} - \boldsymbol{\mu}) \cdot \mathbf{p}'} d\mathbf{p}' \quad (1.19)$$

appearing in (1.18) is a product of sinc functions whose main lobe is at  $\widehat{\mathbf{P}'' - \mathbf{P}'_{n,\alpha}} = \boldsymbol{\mu}$ . When  $\alpha = -$ , the same integral

$$\int_{\text{array}} e^{-ik(\widehat{\mathbf{P}'' - \mathbf{P}'_{n,\alpha}} \cdot \mathbf{p}'_{0,-} - \boldsymbol{\mu} \cdot \mathbf{p}') d\mathbf{p}'} = \int_{\text{array}} e^{-ik(\widehat{\mathbf{P}'' - \mathbf{P}'_{n,\alpha}} - \tilde{\boldsymbol{\mu}}) \cdot \tilde{\mathbf{p}}'} d\tilde{\mathbf{p}}' \quad (1.20)$$

has its main lobe in direction  $\widehat{\mathbf{P}'' - \mathbf{P}'_{n,\alpha}} = \tilde{\boldsymbol{\mu}}$

In some of the cases to follow, it is important to be able to form a beam; in others it is not. In the cases in which it is not, we consider only the field emanating from a single source.

Reception by the array is modeled by integrating the scattered field over the array, again perhaps with some weight for steering.

## 1.2 Monostatic imaging

Work on this part of the project is ongoing, but is close to being finished. The conclusion is that the standard monostatic SAR scenario will give rise to images that have an unacceptable number of artifacts. However, a more workable scenario is to use a fixed array antenna that produces a beam sufficiently narrow to distinguish among different scattering paths. Such measurements can be used to produce images free from artifacts.

## 1.3 Bistatic imaging

We have considered two scenarios: a) a fixed transmitter (perhaps a source of opportunity) and a moving receiver, and b) two independently moving antennas that can both transmit and receive. Our conclusions are that both scenarios lead to images with an unacceptable number of artifacts.

# Chapter 2

## Imaging from high-Doppler-resolution waveforms

This is joint work with Brett Borden. It has been published in [6].

### 2.1 Introduction

Standard synthetic-aperture radar imaging systems [42] transmit wideband waveforms, and the corresponding radar return signals are processed to synthesize the response from a sharp delta-like pulse. Such wideband waveforms are called *high-range-resolution* waveforms because their radar returns can be used to obtain accurate estimates of the distance (range) to a scatterer.

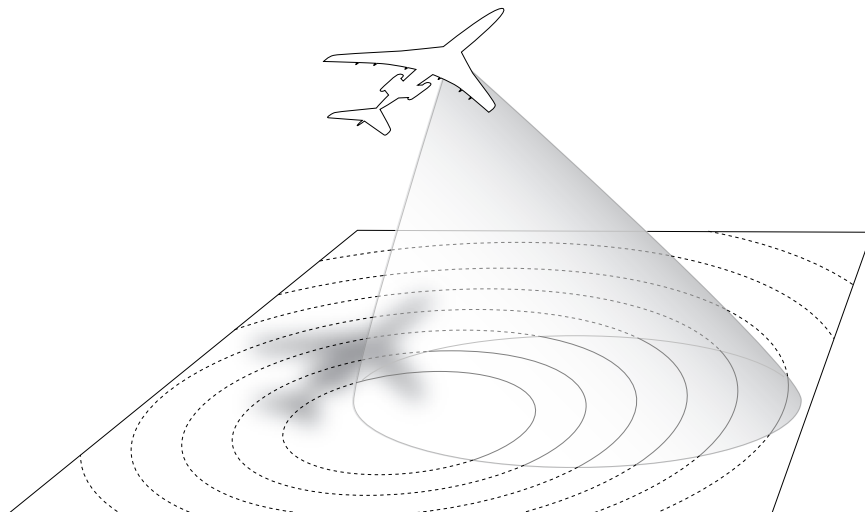


Figure 2.1: A high-range-resolution system.

When a high-range-resolution system is used to image the scatterers on a flat surface, the radar return at each time  $t$  is a superposition of all the returns due to those scatterers positioned at distance  $2t/c$  from the radar. The imaging problem can then be formulated [22, 1, 3, 26] in terms of reconstructing the scattering density function  $\rho$  from its integrals over all circles centered on the flight path of the antenna (see Figure 3.1).

Radar systems can be designed, however, to operate in a complementary mode: instead of transmitting high-range-resolution pulses and estimating target range, they can transmit a high-Doppler-resolution waveform (a fixed-frequency waveform, also called a *continuous-wave* or *CW* waveform) and estimate the relative target velocity from the Doppler frequency shift of the return. For an antenna moving at a constant velocity over a flat surface, the return at a given Doppler shift is a superposition of all the returns due to scatterers with the same relative velocity, and all the scatterers with the same relative velocity lie on a certain hyperbola, called an *iso-Doppler* curve or *isodop*. This suggests a corresponding imaging approach: reconstruct the scattering density function  $\rho$  from its integrals over the iso-Doppler hyperbolas (see Figure 3.2).

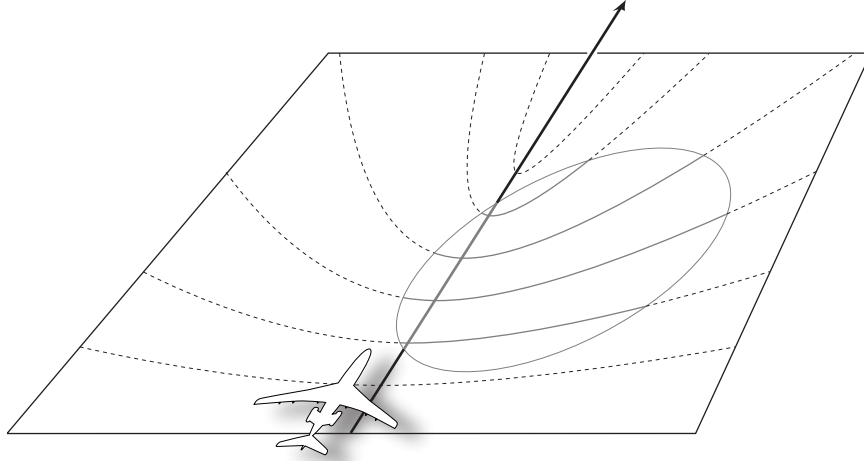


Figure 2.2: A high-Doppler-resolution system.

High-Doppler-resolution imaging systems (which we refer to as simply *Doppler imaging* systems) require only a relatively simple (inexpensive) transmitter and may thus have advantages over high-range-resolution systems in some situations. In addition, Doppler imaging systems may be useful in scenarios in which the radar signals must penetrate through a medium with a frequency-dependent attenuation.

The concept of Doppler imaging is not entirely new. The notion appears in [28]—in the context of a rotating target and stationary radar—to motivate the development of range-Doppler or inverse-synthetic-aperture imaging. The idea is also implicit in the theory of space-time adaptive processing [24]. Moreover, reconstruction of a scattering density function from its integrals over hyperbolas was developed, for wideband range-Doppler radar imaging, in [27]. Doppler imaging of a planar surface, however, does not seem to have been studied in its own right.

The purpose of this paper is to develop the theory of Doppler imaging for the case of a single

sensor moving above a collection of scatterers lying on a surface. In section 2 we set forth our notation and a model for the received radar signal. In section 3 we specialize to the case of a flat earth and constant-velocity flight path. For this case, we develop an approximate image reconstruction algorithm.

## 2.2 Radar data

The basic physics behind radar detection is simple to understand. A time-varying voltage  $s^{in}(t) \in \mathbb{C}$  is passed to a transmitting antenna where it activates a radiating electromagnetic field  $\mathbf{E}^{in}(\mathbf{x}, t) \in \mathbb{C}^3$  defined at spatial position  $\mathbf{x} \in \mathbb{R}^3$  and time  $t$ . This radiating field obeys the vector wave equation and interacts with radar *targets* by inducing time-varying charge distributions  $\mathbf{j}(\mathbf{x}, t)$  on and within their support. In turn, these induced currents establish a response electromagnetic field  $\mathbf{E}^{sc}(\mathbf{x}, t)$  which radiates to a radar receiving antenna where it excites an echo signal voltage  $s^{sc}(t)$  that is fed to the radar receiver. The radar system then uses the known function  $s^{in}(t)$  and the measured function  $s^{sc}(t)$  to estimate various properties of the target that are encoded in  $\mathbf{j}(\mathbf{x}, t)$  (for example, the support of  $\mathbf{j}$  can be used to determine the target's distance and bearing).

The details of the physics underlying the sequence  $s^{in} \rightarrow \mathbf{E}^{in} \rightarrow \mathbf{j} \rightarrow \mathbf{E}^{sc} \rightarrow s^{sc}$  is usually quite complicated and, in practice, various simplifying approximations are applied to keep the analysis tractable.

### 2.2.1 The scattered field

The most common radar echo model is based on a linearized and polarization-insensitive scattering approximation to the electric or magnetic field integral equations. In this *ad hoc* approximation to the electromagnetic scattering problem, we consider only one electric field component, namely the one for which the antenna is designed to be sensitive. The *weak-scatterer* or *Born* approximation takes the induced current  $\mathbf{j}$  to be proportional to the (scalar)  $\tilde{\rho}\ddot{E}^{in}$ , where  $\tilde{\rho}$  is the *target reflectivity function*, and  $\ddot{E}^{in}(\mathbf{z}, t)$  denotes the second time derivative of (one component of) the electric field incident upon the target. The Born-approximated scattered field is given by

$$E_B^{sc}(\mathbf{x}, t) \approx - \iint \frac{\delta(t - t' - |\mathbf{x} - \mathbf{z}|/c_0)}{4\pi|\mathbf{x} - \mathbf{z}|} \tilde{\rho}(\mathbf{z}) \ddot{E}^{in}(\mathbf{z}, t') dt' d\mathbf{z} \quad (2.1)$$

where  $E_B^{sc}(\mathbf{x}, t) \in \mathbb{C}$  denotes the designated component of the scattered electric field. The weak scatterer approximation is well documented in the literature (cf., [4, 5, 28, 39, 42, 45] and references cited therein) and will not be further motivated here.

We assume that the radar emits a continuous wave at the fixed angular frequency  $\omega_0$ . Then the incident field can be expressed in terms of the Green's function for the three dimensional Helmholtz

equation:

$$E^{in}(\mathbf{z}, t) = E_0(\widehat{\mathbf{z} - \mathbf{y}}) \frac{e^{-i\omega_0(t - |\mathbf{z} - \mathbf{y}|/c)}}{4\pi|\mathbf{z} - \mathbf{y}|}, \quad (2.2)$$

where  $\mathbf{y}$  denotes the phase center of the transmitting antenna. Substitution into equation (2.1) yields

$$E_B^{sc}(\mathbf{x}, t) = \frac{\omega_0^2}{(4\pi)^2} \int \tilde{\rho}(\mathbf{z}) \frac{e^{-i(\omega_0/c)(ct - |\mathbf{z} - \mathbf{y}| - |\mathbf{z} - \mathbf{x}|)}}{|\mathbf{z} - \mathbf{y}||\mathbf{z} - \mathbf{x}|} E_0(\widehat{\mathbf{z} - \mathbf{y}}) d\mathbf{z}. \quad (2.3)$$

Below we consider only the case where the transmit and receive antennas are co-located, have the same phase centers and travel along the ight path  $\mathbf{x} = \boldsymbol{\gamma}(t)$ . Moreover, we assume that the scattering takes place in a thin region at the surface  $\mathbf{z} = \boldsymbol{\zeta}(\mathbf{z}_T)$ , where  $\mathbf{z}_T = (z_1, z_2)$ . Thus we write  $\tilde{\rho}(\mathbf{z}) = \rho(\mathbf{z}_T)\delta(\mathbf{z} - \boldsymbol{\zeta}(\mathbf{z}_T))$ . We also introduce the notation:  $\mathbf{R}(\mathbf{z}_T, t) = \boldsymbol{\zeta}(\mathbf{z}_T) - \boldsymbol{\gamma}(t)$ ;  $R(\mathbf{z}_T, t) = |\mathbf{R}(\mathbf{z}_T, t)|$ ; and  $\hat{\mathbf{R}}(\mathbf{z}_T, t) = \mathbf{R}(\mathbf{z}_T, t)/R(\mathbf{z}_T, t)$ . The eld (2.3) is then

$$E_B^{sc}(\boldsymbol{\gamma}(t), t) = \frac{\omega_0^2}{(4\pi)^2} \int \rho(\mathbf{z}_T) \frac{e^{-i\omega_0(t - 2R(\mathbf{z}_T, t))/c}}{R^2(\mathbf{z}_T, t)} E_0(\hat{\mathbf{R}}(\mathbf{z}_T, t)) d\mathbf{z}_T. \quad (2.4)$$

The measured signal voltage  $s^{sc}(t)$  arises from the interaction of  $E^{sc}$  with the antenna and we can write

$$s^{sc}(t) = \frac{\omega_0^2}{(4\pi)^2} \int \rho(\mathbf{z}_T) \frac{e^{-i\omega_0(t - 2R(\mathbf{z}_T, t))/c}}{R^2(\mathbf{z}_T, t)} W(\hat{\mathbf{R}}(\mathbf{z}_T, t)) d\mathbf{z}_T, \quad (2.5)$$

where  $W$  is a weighting factor accounting for the combined transmit and receive antenna patterns [40].

## 2.2.2 Correlation data

The radar receiver correlates the echo signal (2.5) with  $e^{-i\omega t}$ , which is a frequency-shifted version of the incident signal  $s^{in}(t) = e^{-i\omega_0 t}$ , over a nite time window; in other words it measures the windowed Fourier transform. We denote by  $\tilde{\psi}(t - \tau)$  the time windowing function centered at  $t = \tau$ ; we write the (Fourier transform) frequency as  $\omega = \omega_0\mu$ . With this notation the radar data are

$$\begin{aligned} \eta(\tau, \mu) &= \int s^{sc}(t) e^{i\omega_0\mu(t-\tau)} \tilde{\psi}(t - \tau) dt \\ &= \frac{\omega_0^2}{(4\pi)^2} \iint \rho(\mathbf{z}_T) \frac{e^{-i\omega_0(t - 2R(\mathbf{z}_T, t))/c}}{R^2(\mathbf{z}_T, t)} W(\hat{\mathbf{R}}(\mathbf{z}_T, t)) e^{i\omega_0\mu(t-\tau)} \tilde{\psi}(t - \tau) dt d\mathbf{z}_T. \end{aligned} \quad (2.6)$$

Then, using the Taylor expansion

$$\boldsymbol{\gamma}(t) = \boldsymbol{\gamma}(\tau) + \dot{\boldsymbol{\gamma}}(\tau)(t - \tau) + \dots \quad (2.7)$$



to write

$$\begin{aligned} R(\mathbf{z}_T, t) = |\zeta(\mathbf{z}_T) - \gamma(t)| &= |\zeta(\mathbf{z}_T) - \gamma(\tau) - \dot{\gamma}(\tau)(t - \tau) + \dots| \\ &\approx R(\mathbf{z}_T, \tau) - \hat{\mathbf{R}}(\mathbf{z}_T, \tau) \cdot \dot{\gamma}(\tau)(t - \tau), \end{aligned} \quad (2.8)$$

in the exponent of (2.6), we obtain

$$\begin{aligned} \eta(\tau, \mu) &\approx \frac{\omega_0^2}{(4\pi)^2} \iint \rho(\mathbf{z}_T) \frac{e^{-i\omega_0(t-2[R(\mathbf{z}_T, \tau) - \hat{\mathbf{R}}(\mathbf{z}_T, \tau) \cdot \dot{\gamma}(\tau)(t-\tau)]/c)}}{R^2(\mathbf{z}_T, \tau)} \\ &\quad \times W(\hat{\mathbf{R}}(\mathbf{z}_T, t)) e^{i\omega_0\mu(t-\tau)} \tilde{\psi}(t - \tau) dt d\mathbf{z}_T. \end{aligned} \quad (2.9)$$

Finally, in (2.9) we make the change of variables  $t' = t - \tau$  to obtain

$$\eta(\tau, \mu) \approx \iint e^{-i\omega_0 t' (1 - \mu + 2\hat{\mathbf{R}}(\mathbf{z}_T, \tau) \cdot \dot{\gamma}(\tau)/c)} \tilde{A}(\mathbf{z}_T, t', \tau) dt' \rho(\mathbf{z}_T) d\mathbf{z}_T \quad (2.10)$$

where  $t' = t - \tau$  and

$$\tilde{A}(\mathbf{z}_T, t', \tau) = \frac{\omega_0^2 e^{-i\omega_0(\tau - 2R(\mathbf{z}_T, \tau)/c)} \tilde{\psi}(t')}{(4\pi R(\mathbf{z}_T, \tau))^2} W(\hat{\mathbf{R}}(\mathbf{z}_T, t' + \tau)). \quad (2.11)$$

We see that the  $t'$  integration results in an approximate delta function along the curve formed by the intersection of the earth surface with the constant-Doppler cone  $\mu - 1 = 2\hat{\mathbf{R}}(\tau, \mathbf{x}_T) \cdot \dot{\gamma}(\tau)/c$ . When the earth's surface is a flat plane, this curve is a hyperbola.

We use the dimensionless parameter  $\beta = \omega_0 t'$  to write  $A(\mathbf{z}_T, \beta, \tau) = \tilde{A}(\mathbf{z}_T, t', \tau)$  and

$$\varphi(\beta, \mathbf{z}_T, \tau, \mu) = \beta[1 - \mu + 2\hat{\mathbf{R}}(\mathbf{z}_T, \tau) \cdot \dot{\gamma}(\tau)/c] \quad (2.12)$$

so that (2.10) is

$$\eta(\tau, \mu) = \iint A(\mathbf{z}_T, \beta, \tau) e^{-i\varphi(\beta, \mathbf{z}_T, \tau, \mu)} d\beta \rho(\mathbf{z}_T) d\mathbf{z}_T. \quad (2.13)$$

## 2.3 The Case of a Straight Flight Path and Flat Earth

We choose coordinates so that the flight path is along the  $z_1$  axis:  $\gamma(\tau) = (v\tau, 0, H)$ , and we assume that the radar is operating in strip-map mode, meaning that the antenna beam is fixed and side-looking. We assume that the antenna beam illuminates the region  $|z_1 - v\tau| \lesssim \epsilon$ . The phase (2.12) is thus

$$\varphi(\beta, \mathbf{z}_T, \tau, \mu) = \beta \left[ 1 - \mu + \frac{2v}{c} \frac{z_1 - v\tau}{\sqrt{(z_1 - v\tau)^2 + z_2^2 + H^2}} \right] \quad (2.14)$$

$$= \beta \left[ 1 - \mu + \frac{2v/c}{\sqrt{z_2^2 + H^2}}(z_1 - v\tau) + O((z_1 - v\tau)^2) \right]$$

where in the second line of (2.14) we have done a Taylor expansion about the point  $z_1 = v\tau$ . We use the notation  $\tilde{\mu} = \mu - 1$  and use  $\phi$  for the approximate form of the phase:

$$\phi(\beta, \mathbf{z}_T, \tau, \tilde{\mu}) = \beta \left[ -\tilde{\mu} + \frac{2v/c}{\sqrt{(z_2/H)^2 + 1}} \left( \frac{z_1}{H} - \frac{v\tau}{H} \right) \right]. \quad (2.15)$$

The leading-order contribution to  $\eta$  comes from the critical set  $\partial\phi/\partial\beta = 0$ , which, in this approximation, is a straight line in the  $\tilde{\mu}$ - $\tau$  plane. If instead of  $\tau$  we use the dimensionless variable  $\tilde{\tau} = v\tau/H$ , then we find that the straight line in the  $\tilde{\mu}$ - $\tilde{\tau}$  plane has  $\tilde{\tau}$ -intercept  $z_1/H$  and slope  $-2(v/c)((z_2/H)^2 + 1)^{-1/2}$ . We note that  $z_1$  can be found from the  $\tilde{\tau}$ -intercept, and  $z_2$  from the slope.

### 2.3.1 Image formation

We form an image by backprojection:

$$I(\mathbf{y}_T) = \iiint e^{i\phi(\beta, \mathbf{y}_T, \tau, \tilde{\mu})} B(\beta, \mathbf{y}_T, \tau, \tilde{\mu}) d\beta \eta(\tau, \tilde{\mu}) d\tilde{\mu} d\tau \quad (2.16)$$

where  $B$  is to be determined below.

To determine the degree to which the image  $I$  reproduces  $\rho$ , we insert (2.10) into (2.16) and perform a stationary phase reduction in  $\tilde{\mu}$  and one of the  $\beta$  variables. This results in

$$I(\mathbf{y}_T) = \int K(\mathbf{y}_T, \mathbf{z}_T) \rho(\mathbf{z}_T) d\mathbf{z}_T, \quad (2.17)$$

where the point spread function  $K$  is given by

$$K(\mathbf{y}_T, \mathbf{z}_T) = \iint \exp \left( i\beta \frac{2v}{c} \left[ \frac{y_1 - v\tau}{\sqrt{y_2^2 + H^2}} - \frac{z_1 - v\tau}{\sqrt{z_2^2 + H^2}} \right] \right) A(\mathbf{z}_T, \tau) \\ \times B(\beta, \mathbf{y}_T, \tau, \mu(\mathbf{y}_T, \tau)) \psi(\beta) d\beta d\tau \quad (2.18)$$

and where  $\mu(\mathbf{y}_T, \tau) = -(2v/c)(y_1 - v\tau)(y_2^2 + H^2)^{-1/2}$ . We would like to choose  $B$  so that  $K(\mathbf{y}_T, \mathbf{z}_T) = \delta(\mathbf{y}_T - \mathbf{z}_T) = (2\pi)^{-2} \int e^{-i(\mathbf{y}_T - \mathbf{z}_T) \cdot \boldsymbol{\xi}} d\boldsymbol{\xi}$ .

The leading-order contributions to (2.18) come from the critical points of (2.18), which are determined by

$$0 = \frac{\partial\phi}{\partial\beta} \propto \frac{y_1 - v\tau}{\sqrt{y_2^2 + H^2}} - \frac{z_1 - v\tau}{\sqrt{z_2^2 + H^2}},$$

$$0 = \frac{\partial \phi}{\partial \tau} \propto \frac{1}{\sqrt{y_2^2 + H^2}} - \frac{1}{\sqrt{z_2^2 + H^2}}. \quad (2.19)$$

These equations have solutions only when  $(y_1, y_2) = (z_1, \pm z_2)$ , which implies that the only artifacts are the usual left-right ones. (And these artifacts can be avoided by a judicious choice of  $W(\hat{\mathbf{R}}, \tau)$ .)

In (2.18), we expand the phase using the identity

$$f(\mathbf{z}_T) - f(\mathbf{y}_T) = (\mathbf{z}_T - \mathbf{y}_T) \cdot \int_0^1 \nabla f(\mathbf{y}_T + \lambda(\mathbf{z}_T - \mathbf{y}_T)) d\lambda \approx (\mathbf{z}_T - \mathbf{y}_T) \cdot \nabla f(\mathbf{y}_T) \quad (2.20)$$

applied to  $f(\mathbf{y}_T) = (y_1 - v\tau)(y_2^2 + H^2)^{-1/2}$ . We then make the change of variables

$$(\beta, \tau) \rightarrow \boldsymbol{\xi} = (2\beta v/c) \nabla f(\mathbf{y}_T) = \beta \frac{2v}{c} \left( \frac{1}{\sqrt{y_2^2 + H^2}}, \frac{-(y_1 - v\tau)y_2}{(y_2^2 + H^2)^{3/2}} \right)^T \quad (2.21)$$

where the superscript “T” denotes transpose. This converts (2.18) into

$$K(\mathbf{y}_T, \mathbf{z}_T) = \int e^{i(\mathbf{z}_T - \mathbf{y}_T) \cdot \boldsymbol{\xi}} A(\mathbf{z}_T, \tau) B(\beta, \mu(\mathbf{y}_T, \tau), \tau, \mathbf{y}_T) \psi(\beta) \left| \frac{\partial(\beta, \tau)}{\partial \boldsymbol{\xi}} \right| d\boldsymbol{\xi} \quad (2.22)$$

where now  $\beta$  and  $\tau$  are understood to refer to  $\beta(\boldsymbol{\xi})$  and  $\tau(\boldsymbol{\xi})$ . The Jacobian in (2.22) is the reciprocal of

$$\left| \frac{\partial \boldsymbol{\xi}}{\partial(\beta, \tau)} \right| = \frac{4v^2\beta}{c^2} \begin{vmatrix} \frac{1}{\sqrt{y_2^2 + H^2}} & 0 \\ \frac{-(y_1 - v\tau)y_2}{(y_2^2 + H^2)^{3/2}} & \frac{vy_2}{(y_2^2 + H^2)^{3/2}} \end{vmatrix} = \frac{4v^3\beta y_2}{c^2(y_2^2 + H^2)^2}. \quad (2.23)$$

From (2.22), we see that  $B$  should be chosen according to

$$B(\beta, \mu, \tau, \mathbf{y}_T) = \frac{\chi(\beta, \tau, \mathbf{y}_T) \left| \frac{\partial \boldsymbol{\xi}}{\partial(\beta, \tau)} \right|}{(2\pi)^2 A(\mathbf{y}_T, \tau) \psi(\beta)} \quad (2.24)$$

where  $\chi$  is a cutoff function that prevents division by zero in (2.24). With this choice of  $B$ , (2.22) becomes

$$K(\mathbf{y}_T, \mathbf{z}_T) = \frac{1}{(2\pi)^2} \int_{\Xi_{\mathbf{y}}} e^{i(\mathbf{z}_T - \mathbf{y}_T) \cdot \boldsymbol{\xi}} d\boldsymbol{\xi} \quad (2.25)$$

where the integration is over the set  $\Xi_{\mathbf{y}}$  of  $\boldsymbol{\xi}$  swept out according to (2.21) as  $\tau$  and  $\beta$  range over the data collection region for the point  $\mathbf{y}_T$ .

### 2.3.2 Resolution

The resolution of the image (2.16) is determined by the region  $\Xi_{\mathbf{y}}$  of integration in (2.25), which is the set in (2.21) as  $\tau$  and  $\beta$  range over the subset of the data collection region  $[\tau_{\min}, \tau_{\max}] \times$

$[\beta_{\min}, \beta_{\max}]$  that is relevant at the point  $\mathbf{y}_T$ . In particular, the region  $\Xi_{\mathbf{y}}$  is also restricted by the beam pattern  $W$ : the maximum  $X$  of  $x = |y_1 - v\tau|$  is the distance along the right path for which the point  $\mathbf{y}$  remains in the beam. Thus  $x$  is in the interval  $[-X, X]$  where  $X = vT$  with  $T$  being half the persistence interval.

Since  $\beta = \omega_0 t' = \omega_0(t - \tau)$ , the length of the interval  $[\beta_{\min}, \beta_{\max}]$  is  $2\pi$  times the number of cycles in our time window. We write  $\beta_{\min} = -\Omega$  and  $\beta_{\max} = \Omega$ . We assume that the antenna beam is directed to the left of the right path, so that  $y_2 > 0$ .

The boundary of the region  $\Xi$  is formed by the four curves  $\mathcal{C}_\Omega, \mathcal{C}_{-\Omega}, \mathcal{C}_X, \mathcal{C}_{-X}$ :

$$\begin{aligned}\mathcal{C}_{\pm\Omega} &= \{(\xi_1, \xi_2(x)) : \xi_1 = \pm a\Omega, \xi_2 = \pm \Omega bx, x \in [-X, X]\} \\ \mathcal{C}_{\pm X} &= \{\boldsymbol{\xi}(\beta) = (a, \pm Xb)\beta : \beta \in [-\Omega, \Omega]\}\end{aligned}\quad (2.26)$$

where we have written  $a = 2(v/c)(y_2^2 + H^2)^{-1/2}$  and  $b = -2(v/c)y_2(y_2^2 + H^2)^{-3/2}$ .

We see that for a given target location  $(y_1, y_2)$ , the curves  $\mathcal{C}_{\pm\Omega}$  are vertical lines (in which only  $\xi_2$  varies). Similarly, the curves  $\mathcal{C}_{\pm X}$  are radial lines through the origin. The region  $\Xi_{\mathbf{y}}$  is thus a bowtie. The size of  $\Xi_{\mathbf{y}}$  depends not only on the target location  $(y_1, y_2)$  but also on the system parameters  $v, H, \omega_0$ .

To obtain the point spread function (ambiguity function) for a particular image point  $(0, y_2)$ , we calculate the right side of (2.25). We write  $\mathbf{p} = \mathbf{z}_T - \mathbf{y}_T$  in (2.25) and change variables from  $\boldsymbol{\xi} = (a, bx)\beta$  to  $(x, \beta)$ , obtaining

$$K_{\mathbf{y}}(\mathbf{p}) = \frac{1}{(2\pi)^2} \int_{\Xi_{\mathbf{y}}} e^{i\mathbf{p} \cdot \boldsymbol{\xi}} d\boldsymbol{\xi} = \frac{1}{(2\pi)^2} \int_{-\Omega}^{\Omega} \int_{-X}^X e^{i(a,bx) \cdot \mathbf{p}\beta} \left| \frac{\partial \boldsymbol{\xi}}{\partial(\beta, x)} \right| dx d\beta. \quad (2.27)$$

The Jacobian  $|\partial \boldsymbol{\xi} / \partial(\beta, x)|$  is easily found to be equal to  $|ab\beta|$ ;  $K$  can be calculated as follows.

$$\begin{aligned}K_{\mathbf{y}}(\mathbf{p}) &= \frac{-1}{(2\pi)^2} \left( \int_{-\Omega}^0 \int_{-X}^X e^{i(a,bx) \cdot \mathbf{p}\beta} ab\beta dx d\beta - \int_0^{\Omega} \int_{-X}^X e^{i(a,bx) \cdot \mathbf{p}\beta} ab\beta dx d\beta \right) \\ &= \frac{a}{(2\pi)^2 i p_2} \left( \frac{e^{i(a,bX) \cdot \mathbf{p}\Omega} - 1}{i(a, bX) \cdot \mathbf{p}} - \frac{e^{i(a,-bX) \cdot \mathbf{p}\Omega} - 1}{i(a, -bX) \cdot \mathbf{p}} - \frac{1 - e^{-i(a,bX) \cdot \mathbf{p}\Omega}}{i(a, bX) \cdot \mathbf{p}} + \frac{1 - e^{-i(a,-bX) \cdot \mathbf{p}\Omega}}{i(a, -bX) \cdot \mathbf{p}} \right) \\ &= \frac{a}{\pi^2 p_2} \left( \frac{\sin^2((a, bX) \cdot \mathbf{p} \Omega / 2)}{(a, bX) \cdot \mathbf{p}} - \frac{\sin^2((a, -bX) \cdot \mathbf{p} \Omega / 2)}{(a, -bX) \cdot \mathbf{p}} \right). \quad (2.28)\end{aligned}$$

**Down-range resolution.** Down-range resolution is obtained by setting  $p_1 = 0$  in (2.28):

$$K_{\mathbf{y}}(0, p_2) = \frac{a}{\pi^2 p_2} \left( \frac{\sin^2(\Omega b X p_2 / 2)}{b X p_2} - \frac{\sin^2(-\Omega b X p_2 / 2)}{-b X p_2} \right) \propto \frac{\sin^2(\Omega b X p_2 / 2)}{(\Omega b X p_2 / 2)^2}, \quad (2.29)$$

where we have used  $\sin^2 A = \sin^2(-A)$ . From the right side of (2.29), we see that the down-range resolution is

$$\Delta p_2 = \frac{4\pi}{\Omega b X} = \frac{2\pi c(y_2^2 + H^2)^{3/2}}{\Omega X v y_2}, \quad (2.30)$$

where the resolution is defined as the width of the central lobe of (2.29). We see that the down-range resolution is improved by taking a larger synthetic aperture  $2X$ ; this is consistent with our expectation that a single Doppler measurement will provide no range information. Range information is obtained only from combining measurements across the synthetic aperture.

For  $\omega_0 = 2\pi \times 100$  MHz,  $v = 8$  m/s, a 0.5 second time window, and  $y_2 = 400$ , the down-range resolution is roughly  $\Delta p_2 \approx 80$  m.

**Cross-range resolution.** Cross-range or azimuthal resolution is obtained by calculating the  $p_2 \rightarrow 0$  limit of (2.28); this can be done by means of l'Hospital's rule:

$$\begin{aligned}
\lim_{p_2 \rightarrow 0} K_{\mathbf{y}}(p_1, p_2) &\propto \frac{\sin(\Omega a p_1/2) \cos(\Omega a p_1/2)}{\Omega a p_1/2} - \frac{\sin^2(\Omega a p_1/2)}{2(\Omega a p_1/2)^2} \\
&= \frac{1}{\Omega a p_1} \left[ \sin(\Omega a p_1) - \frac{\sin^2(\Omega a p_1/2)}{\Omega a p_1/2} \right] \\
&= \frac{1}{\Omega a p_1} \frac{\sin(\Omega a p_1)}{\Omega a p_1} \left[ \Omega a p_1 - \frac{1 - \cos(\Omega a p_1)}{\sin(\Omega a p_1)} \right] \\
&= \frac{1}{\Omega a p_1} \frac{\sin(\Omega a p_1)}{\Omega a p_1} [\Omega a p_1 - \tan(\Omega a p_1/2)] . \tag{2.31}
\end{aligned}$$

The width of the central lobe of  $K_{\mathbf{y}}(p_1, 0)$  is an estimate of the cross-range resolution and the first zero, which arises from the term in brackets in the last line of (2.31), involves solving the transcendental equation  $\alpha - \tan(\alpha/2) = 0$ ,  $\alpha \neq 0$ . We obtain  $\alpha = 2.33 \dots$ , and so the cross-range resolution is

$$\Delta p_1 \approx \frac{2 \times 2.33}{\Omega a} = \frac{2.33c(y_2^2 + H^2)^{1/2}}{\Omega v} . \tag{2.32}$$

For the same parameter values given above, the cross-range resolution is roughly  $\Delta p_1 \approx 100$  m.

We see that both down-range and cross-range resolution is improved by having a larger number of wave cycles within the time window (i.e., by increasing the frequency  $\omega_0$  or using a longer time window) and increasing the target velocity  $v$ . Resolution is worse for points more distant from the target path.

### 2.3.3 Numerical Implementation

A full implementation of the scheme in section 2.3.1 is, computationally, very expensive. Equation (2.16) is a triple integral with kernel  $B$  given by equation (2.24). Moreover, evaluation of this filtering kernel requires calculation of  $A$  (equation (2.11)) and the Jacobian (equation (2.23)). Even

with the use of look-up tables, the computation requirements associated with such spatially-varying kernels can be daunting.

Instead, we make use of our previous observation: the leading-order contribution to  $\eta$  comes from the critical set  $\partial\phi/\partial\beta = 0$  which, in this approximation, is a straight line in the  $\tilde{\mu}$ - $\tau$  plane. Consequently, an alternative approach can be based on identifying the straight line components in  $\eta(\tau, \tilde{\mu})$ .

An efficient line-detection algorithm makes use of the Radon-Hough transform that integrates over all possible lines:

$$\mathcal{H}\{\eta\}(d, \theta) = \iint \eta(\tau, \tilde{\mu}) \delta(d - \tau \cos \theta - \tilde{\mu} \sin \theta) d\tau d\tilde{\mu}. \quad (2.33)$$

The transform-image of  $\eta$  yields a detected (matched) line's perpendicular offset from the origin  $d$  and the angle  $\theta$  of this offset. The offset  $d$  and angle  $\theta$  are related to the slope  $m$  and  $\tau$ -intercept  $b$  via  $d = b \cos \theta$  and  $m = \tan \theta$ . Because  $\tau$  has the dimensions of time,  $m$  has the dimensions of reciprocal time. These dimensional quantities are related to the dimensionless  $\tilde{\tau}$ -intercept  $\tilde{b}$  and slope  $\tilde{m}$  of the line in the  $\tilde{\mu}$ - $\tilde{\tau}$  plane via  $\tilde{b} = vb/H$  and  $\tilde{m} = Hm/v$ . According to our analysis above, we can therefore form the estimates

$$z_1 = \frac{vd}{\cos \theta} \quad \text{and} \quad \cot \theta = \frac{H}{v} \quad \left( \frac{-c}{2v} \right) \sqrt{\left( \frac{z_2}{H} \right)^2 + 1} \quad (2.34)$$

$$\Rightarrow \quad z_2 = \frac{1}{H} \sqrt{\frac{4v^3 \cot^2 \theta}{H^2 c^2} - 1}$$

to locate the scattering center. Our expedient imaging scheme is therefore performed as a two-step process: 1) form the Radon-Hough transform  $\mathcal{H}\{\eta\}(d, \theta)$  of the correlation data; and 2) map (resample) according to equation (2.34).

Figure 3.7 shows the (magnitude of the) Doppler frequency response of three isolated equal-strength scatterers as a function of time. (The difference in relative strength of each curve is due to a difference in scatterer range.) The simulated data were constructed under the model assumptions of a straight light path for the radar with transmit frequency of  $\omega_0 = 100$  MHz and relative velocity of 8 m/s. Each data point was determined from a 0.5 sec modeled measurement interval (according to equation (2.13)).

Figure 3.8 was formed from the data of Figure 3.7 by resampling the Radon-Hough transform according to equation (2.34). The figure displays the magnitude of the simple transform and no attempt has been made to correct for range-dependent magnitude errors—although this next image processing step could be easily made once the individual scatterer locations have been determined. Figure 3.8 could be improved by image-processing techniques such as high-pass filtering or thresholding. We leave this topic for the future.

We note that Figure 3.8 shows a superposition of three point-spread functions for our expedient imaging scheme.

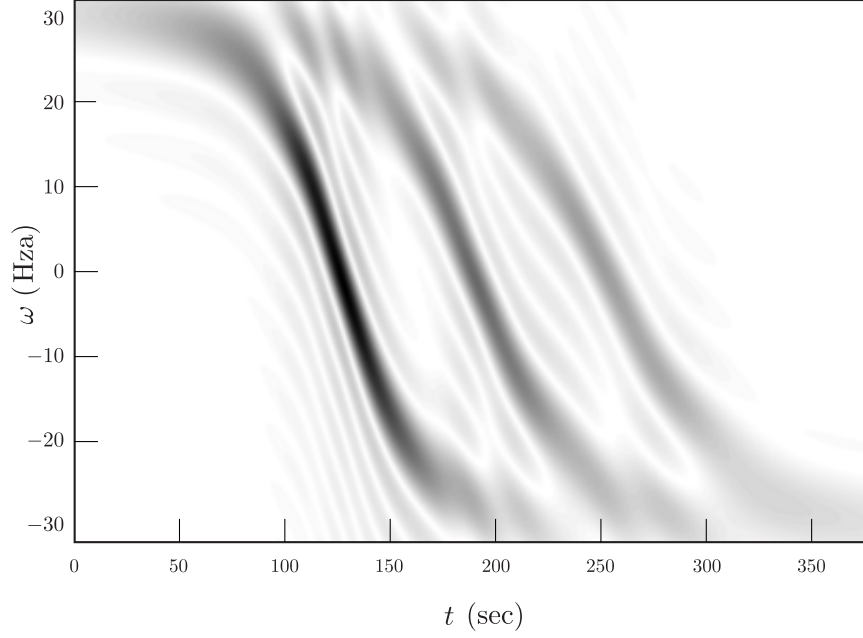


Figure 2.3: The Doppler return from three point scatterers.

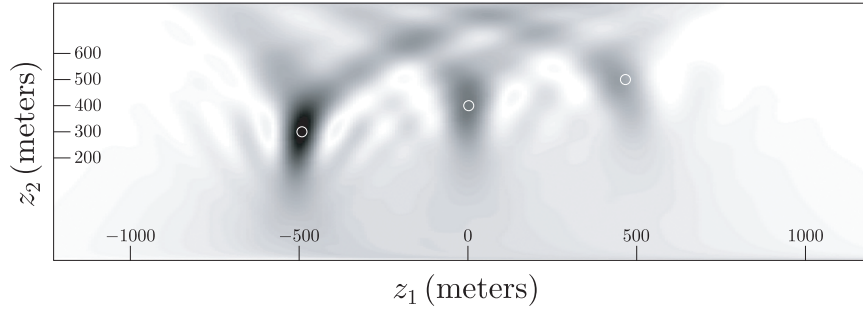


Figure 2.4: The (resampled) Radon-Hough transform of the data in Figure 3.7. The true locations are marked by  $\circ$ ; the right path is along the  $z_1$  axis.

## 2.4 Conclusions and Future Work

We have developed a mathematical model for the radar return signal resulting from a transmitted CW waveform in the case of an antenna moving above a scattering surface. For the case of a right path with constant velocity over a flat surface, we have developed two imaging algorithms. Finally, we have displayed the results of numerical simulation for a simple case.

An important implementation issue that we did not address concerns the difficulty of collecting these data from monostatic systems (in which the transmitter and receiver are co-located). Since the incident wave is constantly transmitting at frequency  $\omega_0$ , any echo wave with zero Doppler shift will be undetectable in the correlation receiver—the echo signal strength will be too small to compete with that of the transmitter. It is conceivable that a judicious choice of antenna weighting

function  $W(\hat{\mathbf{R}})$  combined with frequency domain filtering could be used to “notch-out” this region of the data. Such a notch would need to be sufficiently narrow that only a small fraction of the available data are excluded and, for low frequency systems, the required narrowness of this notch might be impracticable. Of course, this problem is not generally manifest in bistatic systems for which the transmitter and receiver are widely separated and our analysis can be readily modified to include such radar configurations.

Much more work remains to be done, especially for cases in which the geometry is more complicated. In addition we leave for the future the problem of developing fast numerical implementations [32] of the general imaging formula.

## Acknowledgments

This work was supported by the Office of Naval Research, the Air Force Office of Scientific Research under agreement F49620-03-1-0051, and by the Air Force Research Laboratory<sup>1</sup> under agreement FA87500308276. This work was also supported in part by Rensselaer Polytechnic Institute, by the NSF-supported UCLA Institute for Pure and Applied Mathematics, by the NSF Focused Research Groups in the Mathematical Sciences program, and by CenSSIS, the Center for Subsurface Sensing and Imaging Systems, under the Engineering Research Centers Program of the National Science Foundation (award number EEC-9986821).

---

<sup>1</sup>Consequently the U.S. Government is authorized to reproduce and distribute reprints for Governmental purposes notwithstanding any copyright notation thereon. The views and conclusions contained herein are those of the authors and should not be interpreted as necessarily representing the official policies or endorsements, either expressed or implied, of the Air Force Research Laboratory or the U.S. Government.



# Chapter 3

## Imaging that exploits multipath scattering

This work is joint with Bob Bonneau; the theory has been published in [9].

### 3.1 Introduction

This work is motivated by the problem of radar imaging in urban and forested settings. Trees contain branches, which could cause radar reflections; thus an object on the ground could be illuminated not only by waves traveling a direct path from the antenna to the object, but also by waves that have been reflected from branches onto the object. Similarly, imaging in urban settings involves multipath scattering.

Multipath scattering confuses standard imaging methods. However, multiply-reflected waves illuminate the object from a variety of directions; if these waves can be accounted for and used in the imaging process, they might improve the image of the object. This paper provides an imaging method that exploits such multipath scattering. We find that artifacts can arise in certain situations; we show how to avoid them and analyze the improvement in resolution due to the multiply scattered waves. We carry out the details of the analysis explicitly for the case of a single extra scattering path; the extension to more paths is expected to follow along similar lines.

We consider the case in which the multipath scattering is due to the presence of scattering “centers” in the foreground. These scattering centers we model as point scatterers. Such point scatterers are commonly used to model scattering from corners and edges. Using point scatterers has the advantage that an exact closed-form solution is available [37] for multiple scattering between such scatterers.

For scattering from the target or scene of interest, we use the Born (single-scattering) approximation. This approximation neglects multiple scattering within the target and multiple scattering

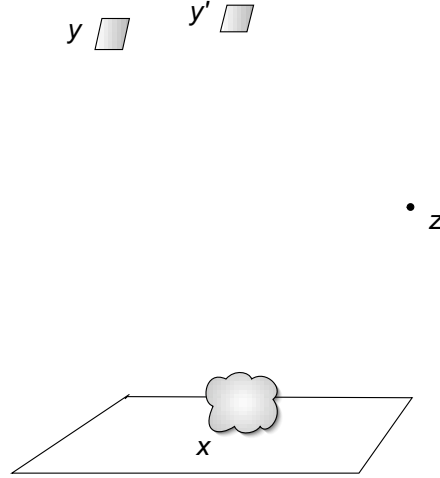


Figure 3.1: Scattering geometry

between the target and its environment; this approximation is ubiquitous in radar work.

In the paper we discuss explicitly the radar case, but the analysis applies equally well to sonar and ultrasound imaging.

The paper is organized as follows. In section 3.2 we develop a mathematical model for the measured signal. We show that this signal is of the form of a Fourier integral operator applied to the scene. In section 3.3 we give a method for producing an image, and show that the image has the desired properties. In section 3.4 we discuss the resolution obtained from this method.

## 3.2 The Mathematical model

The mathematical model involves a number of ingredients: 1) a model for wave propagation in free space, 2) a model for the antenna, 3) a model for multiple scattering from point scatterers in the foreground, and 4) a (linearized) model for scattering from the scene,

### 3.2.1 A model for the wave propagation

Each component of the electromagnetic field propagates in free space according to the scalar wave equation:

$$\nabla^2 u - c^{-2} \ddot{u} = 0, \quad (3.1)$$

where the dots denote differentiation with respect to  $t$ .

Equation (3.1) is not a perfect model for electromagnetic scattering: when electromagnetic waves encounter materials, there is coupling between the different vector components of the electromagnetic field. By using (3.1), we are ignoring such coupling, and we are thus ignoring polarization effects.

We will use capital letters for frequency-domain quantities, which are related to time-domain quantities by the Fourier transform

$$U(\omega, \mathbf{x}) = \frac{1}{2\pi} \int e^{i\omega t} u(t, \mathbf{x}) dt. \quad (3.2)$$

We write  $k = \omega/c_0$ .

We consider the case in which  $N$  scattering “centers” are present in the foreground of the scene we wish to image. These scattering centers we model as point scatterers  $\delta_{\mathbf{z}^j}(\mathbf{x}) = \delta(\mathbf{x} - \mathbf{z}^j)$ ,  $j = 1, 2, \dots, N$ . If we assume that the field  $g_N$  is due to an isotropic point source at position  $\mathbf{y}$  and time  $t = 0$ , the corresponding differential equation is

$$\nabla_{\mathbf{x}}^2 g_N(t, \mathbf{x}, \mathbf{y}) - c_0^{-2} \ddot{g}_N(t, \mathbf{x}, \mathbf{y}) - \sum_{i=1}^N \mu_i \delta_{\mathbf{z}^i}(\mathbf{x}) g_N(t, \mathbf{x}, \mathbf{y}) = -\delta_{\mathbf{y}}(\mathbf{x}) \delta(t) \quad (3.3)$$

Here the  $\mu$ 's are the strengths of the point scatterers. An explicit expression for  $g_N$  is given in the next section.

Behind the cloud of scattering centers is the scene or target we wish to image. We assume that scattering in the scene of interest is due to a perturbation of the wave speed, which we denote by  $q$ .

Whether we can form a three-dimensional image of a volume or merely a two-dimensional image of a surface is determined by the number of degrees of freedom in our measured data. In the case of a (fixed) steerable array antenna, for example, we measure a time-varying field for each steered direction. If the beam can be steered in two directions, we have three degrees of freedom in the data and can expect to make a three-dimensional reconstruction.

In the strip-map synthetic-aperture radar case, however, we measure a time-varying signal from each point along a one-dimensional curve; the data then contains two degrees of freedom and we expect to make only a two-dimensional image of objects sitting on a known surface. In this case, we denote the known surface by  $\{\mathbf{x} = \boldsymbol{\psi}(\mathbf{x}_T) : \mathbf{x}_T \in \mathbb{R}^2\}$ , where  $\mathbf{x}_T = (x_1, x_2)$ , and we write the wave speed perturbation as  $q(\mathbf{x}_T) \delta(\mathbf{x} - \boldsymbol{\psi}(\mathbf{x}_T))$ .

In what follows we consider for simplicity the three-dimensional case; for the two-dimensional case we would simply replace  $\mathbf{x}$  by  $\mathbf{x}_T$  and  $q(\mathbf{x})$  by  $q(\mathbf{x}_T) \delta(\mathbf{x} - \boldsymbol{\psi}(\mathbf{x}_T))$ .

The equation we consider can thus be written

$$\nabla^2 u - c_0^{-2} \ddot{u} - \sum_{i=1}^N \mu_i \delta_{\mathbf{z}^i} u - c_0^{-2} q \ddot{u} = 0 \quad (3.4)$$

In (3.4),  $q$  is the quantity we wish to reconstruct.

### 3.2.2 A model for the antenna

We model the antenna as an array antenna in which each element is an isotropic radiator. At frequency  $\omega$ , the eld at  $\mathbf{x}$  emanating from the element at  $\mathbf{y}$  is  $G_0(\omega, |\mathbf{x} - \mathbf{y}|)$ , where  $G_0(\omega, r) = (4\pi r)^{-1} \exp(ikr)$ . To model the eld  $u$  from an extended antenna, centered at  $\mathbf{y}$ , over which the derivative of the current density is  $j(t, \mathbf{y}')$ , where  $\mathbf{y}'$  denotes a vector from the center  $\mathbf{y}$  to an arbitrary point on the antenna, we simply integrate:

$$u(t, \mathbf{x}) = \int_{-\infty}^{\infty} e^{-i\omega t} \int_{\text{antenna}} G_0(\omega, |\mathbf{x} - (\mathbf{y} + \mathbf{y}')|) J(\omega, \mathbf{y}') d\mathbf{y}' d\omega. \quad (3.5)$$

(Here  $J$  denotes the Fourier transform of  $j$ .)

A steered antenna beam can be modeled by including phasing in  $j$ . For example, for a beam steered in direction  $\boldsymbol{\mu}$ , one can choose  $J_{\boldsymbol{\mu}}(\omega, \mathbf{y}') = \exp(-i\omega \boldsymbol{\mu} \cdot \mathbf{y}') \chi_{\text{antenna}}(\mathbf{y}')$ , where  $\chi_{\text{antenna}}$  denotes a function that is one on the antenna and zero off it.

In what follows, we consider only the eld  $G_0$  emanating from a single antenna element, with the understanding that these elds can be assembled to model any desired antenna.

Reception by the antenna is modeled by integrating the scattered eld over the antenna, again perhaps with some weight for steering. For simplicity we consider only the

### 3.2.3 Multiple scattering from point scatterers

For a time-harmonic incident wave  $U^{\text{in}}$ , the frequency-domain eld  $U^{\text{sc}}$  scattered from  $N$  “point” scatterers can be obtained from the Foldy-Lax [45] equations together with the assumption that the scattered eld from an individual “point” scatterer is proportional to the free-space Green’s function  $G_0$  [37]:

$$U^{\text{sc}}(\omega, \mathbf{x}) = \sum_{j=1}^N G_0(\omega, |\mathbf{x} - \mathbf{z}^j|) \mu_j U_j(\omega, \mathbf{z}^j) \quad (3.6)$$

$$U_j(\omega, \mathbf{x}) = U^{\text{in}}(\omega, \mathbf{x}) + \sum_{i \neq j} G_0(\omega, |\mathbf{x} - \mathbf{z}^i|) \mu_i U_i(\omega, \mathbf{z}^i), \quad j = 1, 2, \dots, N, \quad (3.7)$$

Equation (3.6) says that the scattered eld is the sum of the elds scattered from each scatterer; moreover, the eld scattered from the  $j$ th scatterer is proportional to the eld  $U_j$  that is incident upon the  $j$ th scatterer. Equations (3.7) say that the  $j$ th local incident eld is the overall incident eld plus the eld scattered from all the other scatterers. If the scattering strengths  $\mu_1, \mu_2, \dots, \mu_N$  and positions  $\mathbf{z}^1, \mathbf{z}^2, \dots, \mathbf{z}^N$  are known, the equations (3.7) can be solved for the  $U_j$ ; then the total eld  $U = U^{\text{inc}} + U^{\text{sc}}$  can be found from (3.6).

The total field  $U$  satisfies the “background” differential equation

$$\nabla^2 U + k^2 U + \sum_{i=1}^N \mu_i \delta_{\mathbf{z}^i} U = 0 \quad (3.8)$$

where  $k = \omega/c_0$ . We note that the sense in which a field of the form (3.6) satisfies (3.8) requires an extension of the traditional distributional definition of the delta function; its domain must be extended to include functions with  $1/r$  singularities. A thorough discussion of this issue can be found in [2].

We will write  $G_N$  for the full field  $U$  in the case when  $U^{\text{inc}} = G_0$ .

### Example: A single point scatterer

For a single point scatterer located at position  $\mathbf{z}$ , the scattered field is simply

$$U^{\text{m}}(\mathbf{x}) = k^2 G_0(|\mathbf{x} - \mathbf{z}|) \mu U^{\text{in}}(\mathbf{z}) \quad (3.9)$$

The corresponding time-domain scattered field is

$$u^{\text{m}}(t, \mathbf{x}) = \int e^{-i\omega t} G_0(\omega, |\mathbf{x} - \mathbf{z}|) \mu U^{\text{in}}(\omega, \mathbf{z}) d\omega. \quad (3.10)$$

We obtain the one-point-scatterer “background” Green’s function  $G_1$  by taking  $U^{\text{in}} = G_0$ :

$$G_1(\omega, \mathbf{x}, \mathbf{y}') = G_0(\omega, |\mathbf{x} - \mathbf{y}'|) + G_0(\omega, |\mathbf{x} - \mathbf{z}|) \mu G_0(\omega, |\mathbf{z} - \mathbf{y}'|) \quad (3.11)$$

We will denote the second term on the right side of (3.11) by  $G_1^{\text{sc}}$ .

### Example: A pair of point scatterers

In the case of two “point” scatterers, equations (3.7) are

$$U_1(\mathbf{x}) = U^{\text{in}}(\mathbf{x}) + G_0(|\mathbf{x} - \mathbf{z}^1|) \mu_2 U_2(\mathbf{z}^2) \quad (3.12)$$

$$U_2(\mathbf{x}) = U^{\text{in}}(\mathbf{x}) + G_0(|\mathbf{x} - \mathbf{z}^2|) \mu_1 U_1(\mathbf{z}^1) \quad (3.13)$$

Evaluating (3.12) at  $\mathbf{z}^1$  and (3.13) at  $\mathbf{z}^2$  gives rise to the system of equations

$$\begin{pmatrix} 1 & -\mu_2 G_0(L) \\ -\mu_1 G_0(L) & 1 \end{pmatrix} \begin{pmatrix} U_1(\mathbf{z}^1) \\ U_2(\mathbf{z}^2) \end{pmatrix} = \begin{pmatrix} U^{\text{inc}}(\mathbf{z}^1) \\ U^{\text{inc}}(\mathbf{z}^2) \end{pmatrix}, \quad (3.14)$$

where  $L = |\mathbf{z}^2 - \mathbf{z}^1|$ . These equations have the solutions

$$U_j(\mathbf{z}^j) = \frac{U^{\text{inc}}(\mathbf{z}^j) + \mu_{j'} G_0(L) U^{\text{inc}}(\mathbf{z}^{j'})}{1 - \mu_1 \mu_2 G_0^2(L)}, \quad j = 1, 2, \quad (3.15)$$

where  $j' = 2$  if  $j = 1$  and  $j' = 1$  if  $j = 2$ . Using (3.15) in (3.6) yields

$$U^{\text{sc}}(\mathbf{x}) = \sum_{j=1}^2 G_0(|\mathbf{x} - \mathbf{z}^j|) \mu_j \frac{U^{\text{inc}}(\mathbf{z}^j) + \mu_{j'} G_0(L) U^{\text{inc}}(\mathbf{z}^{j'})}{1 - \mu_1 \mu_2 G_0^2(L)}. \quad (3.16)$$

Equation (3.16) has a clear physical interpretation if we consider the denominator to be the sum of a geometric series:

$$\begin{aligned} U^{\text{sc}}(\mathbf{x}) = & \sum_{j=1}^2 \left[ G_0(|\mathbf{x} - \mathbf{z}^j|) \mu_j \sum_{n=0}^{\infty} [\mu_1 \mu_2 G_0^2(L)]^n U^{\text{inc}}(\mathbf{z}^j) \right. \\ & \left. + G_0(|\mathbf{x} - \mathbf{z}^j|) \mu_j \mu_{j'} G_0(L) \sum_{n=0}^{\infty} [\mu_1 \mu_2 G_0^2(L)]^n U^{\text{inc}}(\mathbf{z}^{j'}) \right] \end{aligned} \quad (3.17)$$

The  $n = 0$  term on the first line of (3.17) corresponds to the incident wave scattering once from  $\mathbf{z}^j$ ; the  $n = 0$  terms on the second line corresponds to the incident wave scattering once from  $\mathbf{z}^{j'}$  and once from  $\mathbf{z}^j$ . The  $n = 1$  term on the first line corresponds to initial scattering from  $\mathbf{z}^j$ , then from  $\mathbf{z}^{j'}$ , and then from  $\mathbf{z}^j$  again. The  $n = 1$  term on the second line corresponds to initial scattering from  $\mathbf{z}^{j'}$  and two bounces off  $\mathbf{z}^j$ . The terms corresponding to larger values of  $n$  have similar interpretations.

In any physical problem, some energy loss occurs with each bounce (modeled by the  $\mu$ 's being less than one), so that only a few terms in the series are relevant.

The two-point-scatterer “background” Green’s function  $G_2$  is found by taking  $U^{\text{inc}} = G_0$ :

$$\begin{aligned} G_2(\omega, \mathbf{x}, \mathbf{y}') = & G_0(\omega, \mathbf{x}, \mathbf{y}') + \sum_{j=1}^2 G_0(\omega, |\mathbf{x} - \mathbf{z}^j|) \mu_j \\ & \times \frac{G_0(\omega, |\mathbf{z}^j - \mathbf{y}'|) + \mu_{j'} G_0(\omega, L) G_0(\omega, |\mathbf{z}^{j'} - \mathbf{y}'|)}{1 - \mu_1 \mu_2 G_0^2(\omega, L)} \end{aligned} \quad (3.18)$$

## **$N$ point scatterers**

When  $N$  scatterers are present, (3.7) is a system of  $N$  equations that can be solved by Cramer’s rule, which results in a complicated but closed-form expression for the solution. This expression has a denominator containing the determinant of coefficients; this determinant has an expansion that allows for a multipath interpretation similar to the one above. As before, only a limited number of terms need to be retained.

### 3.2.4 The model for scattering from the target

The total field  $G(\omega, \mathbf{y}, \mathbf{y}')$  at  $\mathbf{y}$  due to the antenna element at  $\mathbf{y}'$  is equal to the sum of the following fields: a) the free-space field  $G_0(\omega, |\mathbf{y} - \mathbf{y}'|)$  emanating from the antenna element, b) the field  $G_N$  scattered from the  $N$  point scatterers in the foreground, and c) the field  $G^{\text{sc}}$  scattered from the target  $q(\mathbf{x})$ .

For  $G^{\text{sc}}$ , we use the *Born approximation* or *single-scattering* approximation to model the scattered field.

The Born approximation in this case is

$$G_B^{\text{sc}}(\omega, \mathbf{y}, \mathbf{y}') = - \int G_N(\omega, \mathbf{y}, \mathbf{x}) q(\mathbf{x}) G_N(\omega, \mathbf{x}, \mathbf{y}') \omega^2 d\mathbf{x}. \quad (3.19)$$

The Born approximation makes the mapping from  $q$  to  $u^{\text{sc}}$  linear, but it is not necessarily a good approximation. Another linearizing approximation that can be used for reflection from smooth surfaces is the *Kirchhoff approximation*, in which the scattered field is replaced by its geometrical optics approximation [8] [25]. Here, however, we consider only the Born approximation.

The corresponding time-domain field is

$$g_B^{\text{sc}}(t, \mathbf{y}, \mathbf{y}') = \int e^{-i\omega t} G_N(\omega, \mathbf{y}, \mathbf{x}) q(\mathbf{x}) G_N(\omega, \mathbf{x}, \mathbf{y}') \omega^2 d\mathbf{x} d\omega. \quad (3.20)$$

We note that this field is of the form

$$g_B^{\text{sc}}(t, \mathbf{y}, \mathbf{y}') = \sum_{j \in \{\text{paths}\}} F_j[q](t, \mathbf{y}, \mathbf{y}') \quad (3.21)$$

where

$$F_j[q](t, \mathbf{y}, \mathbf{y}') = \int e^{-i\omega[t - \tau_j(\mathbf{y}, \mathbf{y}', \mathbf{x})]} a_j(\omega, \mathbf{y}, \mathbf{y}', \mathbf{x}) d\omega q(\mathbf{x}) d\mathbf{x} \quad (3.22)$$

where  $\tau_j$  denotes the travel time along path  $j$  and where  $a_j$  contains the geometrical spreading factors, multiples of  $4\pi$ , and (the Fourier transform of) the waveform sent to the antenna.

The total field is  $G = G_0 + G_N + G^{\text{sc}} \approx G_0 + G_N + G_B^{\text{sc}}$ .

## 3.3 Image formation

We outline first the strategy for the general case of  $N$  point scatterers, then carry out the detailed analysis for the case of a single point scatterer.

### 3.3.1 General strategy

We assume the source location  $\mathbf{y}'$  and receiver location  $\mathbf{y}$  are known; thus  $G_0(\omega, \mathbf{y}, \mathbf{y}')$  can be subtracted from the received field. This leaves  $G_r = G - G_0$ , which we consider to be the data in the image formation process.

The next step in the image formation process is to identify the foreground scatterers. This can be done from the early-time part ( $G_N$ ) of the signal, because the scatterers are assumed to be in front of the scene of interest. Identification of the locations  $\mathbf{z}^j$  and strengths  $\mu_j$  from  $G_N$  can be done in a number of ways. One approach is to use optimization, in which one finds the  $\mathbf{z}$ 's and  $\mu$ 's that minimize

$$\min_{\mathbf{z}^j, \mu_j} \|G_N^{\text{measured}} - G_N^{\text{calculated}}\|. \quad (3.23)$$

Another approach for finding the locations  $\mathbf{z}^j$  is to use Devaney's MUSIC algorithm [17]. Although the treatment in [17] is based on the Born approximation, in fact Devaney's approach applies also to the multiple-scattering case: determining the locations of the point scatterers depends only on the fact that (3.6) is a linear combination of the functions  $G_0(\omega, |\mathbf{x} - \mathbf{z}^j|)$ .

Once the locations and strengths of the foreground scatterers are known, then  $G_N$  is known and can be subtracted out. This leaves  $G^{\text{sc}}$ , from which we form an image by filtered backprojection:

$$I(\mathbf{p}) = B[g^{\text{sc}}](\mathbf{p}) := \sum_{j \in \{\text{paths}\}} \int e^{i\omega[t - \tau_j(\mathbf{y}, \mathbf{y}', \mathbf{p})]} b_j(\omega, \mathbf{p}, \mathbf{y}, \mathbf{y}') g^{\text{sc}}(t, \mathbf{y}, \mathbf{y}') dt d\mathbf{y} d\mathbf{y}' \quad (3.24)$$

where the filters  $b_j$  are determined below. We note that in (3.24), the paths are known because the foreground scatterers are known. We see below that we must take precautions to avoid artifacts in the image.

In (3.24) the integration over  $\mathbf{y}$  and  $\mathbf{y}'$  indicates that we sum over all the data. As written, (3.24) is appropriate for a collection of isotropically-radiating sources and receivers; in the case of a single steered antenna, we would integrate instead over the steering vectors  $[\mu$  in the notation of (3.5)] for the transmitted and received fields. We see below that in order to avoid artifacts, we backproject only along paths that include a direct path to (or from) the scatterer.

We illustrate the imaging process and its analysis for the case of one foreground point scatterer.

### 3.3.2 Case of a single point scatterer

For the case of a single point scatterer at position  $\mathbf{z}$ , the Born-approximated field  $G_B$  is of the form

$$g_B(t, \mathbf{y}, \mathbf{y}') = g_1(t, \mathbf{y}, \mathbf{y}') + \int e^{-i\omega t} G_1(\omega, \mathbf{y}, \mathbf{x}) q(\mathbf{x}) G_1(\omega, \mathbf{x}, \mathbf{y}') \omega^2 d\omega d\mathbf{x}$$



$$\begin{aligned}
&= g_0 + g_1^{\text{sc}} + \int e^{-i\omega t} (G_0 + G_1^{\text{sc}}) q (G_0 + G_1^{\text{sc}}) \omega^2 d\omega d\mathbf{x} \\
&= g_0 + g_1^{\text{sc}} + (F_1 + F_2 + F_3 + F_4)[q]
\end{aligned} \tag{3.25}$$

where  $G_1$  is given by (3.11), where  $G_1^{\text{sc}} = G_1 - G_0$ , and where the operators  $F_j$  are

$$\begin{aligned}
F_1[q](t, \mathbf{y}, \mathbf{y}') &= \int e^{-i\omega t} G_0(\omega, \mathbf{y}, \mathbf{x}) G_0(\omega, \mathbf{x}, \mathbf{y}') q(\mathbf{x}) d\mathbf{x} \\
F_2[q](t, \mathbf{y}, \mathbf{y}') &= \int e^{-i\omega t} G_1^{\text{sc}}(\omega, \mathbf{y}, \mathbf{x}) G_0(\omega, \mathbf{x}, \mathbf{y}') q(\mathbf{x}) d\mathbf{x} \\
F_3[q](t, \mathbf{y}, \mathbf{y}') &= \int e^{-i\omega t} G_0(\omega, \mathbf{y}, \mathbf{x}) G_1^{\text{sc}}(\omega, \mathbf{x}, \mathbf{y}') q(\mathbf{x}) d\mathbf{x} \\
F_4[q](t, \mathbf{y}, \mathbf{y}') &= \int e^{-i\omega t} G_1^{\text{sc}}(\omega, \mathbf{y}, \mathbf{x}) G_1^{\text{sc}}(\omega, \mathbf{x}, \mathbf{y}') q(\mathbf{x}) d\mathbf{x}
\end{aligned} \tag{3.26}$$

The different  $F$ 's correspond to different scattering paths:  $F_1$  corresponds to the direct path from  $\mathbf{y}'$  to the target to  $\mathbf{y}$ ;  $F_2$  corresponds to the path for which a wave leaves  $\mathbf{y}'$ , scatters from the foreground scatterer at  $\mathbf{z}$  onto the target, and takes a direct path back to  $\mathbf{y}$ ; etc. The corresponding travel times  $\tau_j$  for these paths are

$$\begin{aligned}
\tau_1(\mathbf{y}, \mathbf{y}', \mathbf{p}) &= |\mathbf{y} - \mathbf{x}| + |\mathbf{x} - \mathbf{y}'| \\
\tau_2(\mathbf{y}, \mathbf{y}', \mathbf{p}) &= |\mathbf{y} - \mathbf{z}| + |\mathbf{z} - \mathbf{x}| + |\mathbf{x} - \mathbf{y}'| \\
\tau_3(\mathbf{y}, \mathbf{y}', \mathbf{p}) &= |\mathbf{y} - \mathbf{x}| + |\mathbf{x} - \mathbf{z}| + |\mathbf{z} - \mathbf{y}'| \\
\tau_4(\mathbf{y}, \mathbf{y}', \mathbf{p}) &= |\mathbf{y} - \mathbf{z}| + 2|\mathbf{x} - \mathbf{z}| + |\mathbf{z} - \mathbf{y}'|
\end{aligned} \tag{3.27}$$

## Identification of scatterer in the foreground

We assume that the foreground point scatterers are closer to the sensor than the object  $q$  and that therefore the early-time part of (3.25) consists only of the term  $g_1(t, \mathbf{y}, \mathbf{y}')$ . Since we know  $\mathbf{y}$  and  $\mathbf{y}'$ , we can subtract out  $g_0$  from  $g_1$ , leaving

$$\begin{aligned}
g_1^{\text{sc}}(t, \mathbf{y}, \mathbf{y}') &= \int e^{-i\omega t} G_0(\omega, |\mathbf{y} - \mathbf{z}|) \mu G_0(\omega, |\mathbf{z} - \mathbf{y}'|) d\omega \\
&= \mu \int \frac{e^{-i\omega[t - |\mathbf{y} - \mathbf{z}| - |\mathbf{z} - \mathbf{y}'|]}}{(4\pi)^2 |\mathbf{y} - \mathbf{z}| |\mathbf{z} - \mathbf{y}'|} d\omega
\end{aligned} \tag{3.28}$$

In the case of a single point scatterer, there can be no multiple scattering, which implies that the field  $g_1$  is the same as its Born approximation. We can thus form an image of the scatterer  $\mathbf{z}$  by backprojection as described below for the  $i = 1$  case.

## Backprojection

We form the image  $I$  by means of (3.24). In the analysis below, we replace  $g^{\text{sc}}$  by  $g_B^{\text{sc}}$ . If, in (3.24), we naively backproject along all possible paths, we will see that some paths cause artifacts in the image.

Using  $g^{\text{sc}} \approx \sum_j F_j[q]$  [from (3.22)] in (3.24) results in an equation of the form

$$I(\mathbf{p}) \approx \sum_{i=1}^4 \sum_{j=1}^4 B_i[F_j[q]](\mathbf{p}) = \int K(\mathbf{p}, \mathbf{x}) q(\mathbf{x}) d\mathbf{x}, \quad (3.29)$$

where the kernel  $K$  is the imaging *point-spread function*. If we had  $K(\mathbf{p}, \mathbf{x}) = \delta(\mathbf{p} - \mathbf{x})$ , then the image  $I$  would be perfect; we want to determine the  $b_j$  so that  $K$  comes as close as possible to being a delta function.

The contribution to  $K$  from  $B_i F_j$  is

$$K_{i,j}(\mathbf{p}, \mathbf{x}) = \int e^{i\omega(t - \tau_i(\mathbf{y}, \mathbf{y}', \mathbf{p}))} b_i(\omega, \mathbf{p}, \mathbf{y}, \mathbf{y}') \times e^{-i\omega'(t - \tau_j(\mathbf{y}, \mathbf{y}', \mathbf{x}))} a_j(\omega', \mathbf{y}, \mathbf{y}', \mathbf{x}) d\omega d\omega' dt d\mathbf{y} d\mathbf{y}' \quad (3.30)$$

In (3.30) we carry out the  $t$  and  $\omega'$  integrations, obtaining

$$K_{i,j}(\mathbf{p}, \mathbf{x}) = 2\pi \int e^{i\omega(\tau_j(\mathbf{y}, \mathbf{y}', \mathbf{x}) - \tau_i(\mathbf{y}, \mathbf{y}', \mathbf{p}))} b_i(\omega, \mathbf{p}, \mathbf{y}, \mathbf{y}') a_j(\omega, \mathbf{y}, \mathbf{y}', \mathbf{x}) d\omega d\mathbf{y} d\mathbf{y}' \quad (3.31)$$

In order for the  $K$  to be a close approximation to a delta function, we would like the diagonal terms  $K_{i,i}$  themselves to be good approximations to delta functions, and we would like the off-diagonal terms  $K_{i,j}$ ,  $i \neq j$  to be zero or to contribute only higher-order terms. To determine whether this is the case, we analyze each term.

In each case, the analysis is similar: we use the method of stationary phase (see appendix) to determine the leading-order contributions. Analysis of the critical points of the phase determines the locus of points  $\mathbf{p}$  that will appear in the image due to a scatterer located at  $\mathbf{x}$ . We would like the critical conditions to imply that  $\mathbf{p} = \mathbf{x}$ ; if this is not the case, the other possible solutions  $\mathbf{p}$  tell us what artifacts will appear in the image due to a scatterer at  $\mathbf{x}$ .

Analysis of the critical conditions determine *where* in the image a scatterer at  $\mathbf{x}$  is positioned; the coefficients  $b_i$  determine the *amplitude* of the image at  $\mathbf{x}$ . The coefficients  $b_i$  we determine from the diagonal terms  $K_{i,i}$ . In these diagonal terms, we make a change of variables so that the phase of  $K_{i,i}$  is the phase of a delta function. Then, we determine  $b_i$  by the criterion that in order for  $K_{i,i}$  to best approximate a delta function, its amplitude should be  $(2\pi)^{-3}$ .

**The term  $K_{1,1}$ .**

The phase of  $K_{1,1}$  is

$$\begin{aligned} \phi_{1,1}(\omega, \mathbf{y}, \mathbf{y}', \mathbf{p}, \mathbf{x}) &= \omega(\tau_1(\mathbf{y}, \mathbf{y}', \mathbf{x}) - \tau_1(\mathbf{y}, \mathbf{y}', \mathbf{p})) \\ &= \omega[ (|\mathbf{y} - \mathbf{x}| + |\mathbf{x} - \mathbf{y}'|) - (|\mathbf{y} - \mathbf{p}| + |\mathbf{p} - \mathbf{y}'|) ] \end{aligned} \quad (3.32)$$

By a stationary-phase calculation, the leading-order contribution to  $K_{1,1}$  comes from the stationary points at which  $0 = \partial_\omega \phi_{1,1} = \partial_{\mathbf{y}} \phi_{1,1} = \partial_{\mathbf{y}'} \phi_{1,1}$ . These stationary points satisfy

$$\begin{aligned} 0 = \partial_\omega \phi_{1,1} &= [(|\mathbf{y} - \mathbf{x}| + |\mathbf{x} - \mathbf{y}'|) - (|\mathbf{y} - \mathbf{p}| + |\mathbf{p} - \mathbf{y}'|)] \\ 0 = \partial_{\mathbf{y}} \phi_{1,1} &= \widehat{(\mathbf{y} - \mathbf{x})} - \widehat{(\mathbf{y} - \mathbf{p})} \\ 0 = \partial_{\mathbf{y}'} \phi_{1,1} &= \widehat{(\mathbf{x} - \mathbf{y}')} - \widehat{(\mathbf{p} - \mathbf{y}')} \end{aligned} \quad (3.33)$$

where the hats denote unit vectors. The first equation of (3.33) says that  $\mathbf{p}$  must lie on the same equal-travel-time ellipse as  $\mathbf{x}$ ; the second and third equations say that the directions from  $\mathbf{y}$  to  $\mathbf{x}$  and  $\mathbf{p}$  must be the same. Clearly the only point satisfying all these conditions is  $\mathbf{p} = \mathbf{x}$ .

We note that the form taken by the critical conditions depends on the measurement geometry. The above analysis assumes a rather unusual situation, namely that the transmitters  $\mathbf{y}'$  and receivers  $\mathbf{y}$  are spread continuously over a three-dimensional region. A more common arrangement is for the sources and receivers to form a planar array antenna; in this case the integration in (3.31) is only over the two-dimensional array, and the differentiations to determine the critical points are only two-dimensional. For an array antenna, the second line of (3.33) is replaced by  $\widehat{(\mathbf{y} - \mathbf{x})}_T = \widehat{(\mathbf{y} - \mathbf{p})}_T$  where the subscripts  $T$  denote the projection onto the two-dimensional array plane for the receiver. Similarly the third line of (3.33) is replaced by a projection onto the array plane of the transmitter. We note that the two-dimensional projection of a unit vector determines the unit vector in the case we have here, in which we know the unit vector is pointing downwards. (Physically the fact that the two-dimensional projection determines the unit vector corresponds to the fact that an array antenna can produce a steered beam.) Thus the critical equations for the two-dimensional array configuration imply the equations for the three-dimensional measurement geometry. For simplicity of notation, we write simply  $\mathbf{y}$  and  $\mathbf{y}'$  for the positions of the array elements, keeping in mind that these might vary over only a two-dimensional surface.

**The term  $K_{1,2}$ .**

The phase of  $K_{1,2}$  is

$$\begin{aligned} \phi_{1,2}(\omega, \mathbf{y}, \mathbf{y}', \mathbf{p}, \mathbf{x}) &= \omega(\tau_2(\mathbf{y}, \mathbf{y}', \mathbf{x}) - \tau_1(\mathbf{y}, \mathbf{y}', \mathbf{p})) \\ &= \omega[(|\mathbf{y} - \mathbf{z}| + |\mathbf{z} - \mathbf{x}| + |\mathbf{x} - \mathbf{y}'|) - (|\mathbf{y} - \mathbf{p}| + |\mathbf{p} - \mathbf{y}'|)] \end{aligned} \quad (3.34)$$

The stationary points satisfy

$$\begin{aligned} 0 = \partial_\omega \phi_{1,2} &= (|\mathbf{y} - \mathbf{z}| + |\mathbf{z} - \mathbf{x}| + |\mathbf{x} - \mathbf{y}'|) - (|\mathbf{y} - \mathbf{p}| + |\mathbf{p} - \mathbf{y}'|) \\ 0 = \partial_{\mathbf{y}} \phi_{1,2} &= \widehat{(\mathbf{y} - \mathbf{z})} - \widehat{(\mathbf{y} - \mathbf{p})} \\ 0 = \partial_{\mathbf{y}'} \phi_{1,2} &= \widehat{(\mathbf{x} - \mathbf{y}')} - \widehat{(\mathbf{p} - \mathbf{y}')} \end{aligned} \quad (3.35)$$

The second equation of (3.35) says that  $\mathbf{p}$  must lie along the line joining  $\mathbf{z}$  and  $\mathbf{y}$ . If this is the case, then  $|\mathbf{y} - \mathbf{z}| - |\mathbf{y} - \mathbf{p}| = |\mathbf{z} - \mathbf{p}|$ . The first equation of (3.35) then becomes

$$|\mathbf{z} - \mathbf{x}| + |\mathbf{x} - \mathbf{y}'| = |\mathbf{z} - \mathbf{p}| + |\mathbf{p} - \mathbf{y}'| \quad (3.36)$$

which shows that  $\mathbf{p}$  must lie on the same ellipsoid as  $\mathbf{x}$ . The third equation of (3.35) specifies that the  $\mathbf{p}$  must be in the same direction from  $\mathbf{y}'$  as  $\mathbf{x}$ ; thus  $\mathbf{p} = \mathbf{x}$ . In other words, all conditions of (3.35) are satisfied when  $\mathbf{p} = \mathbf{x}$  and  $\mathbf{x}$  lies directly behind  $\mathbf{z}$  when viewed from the position  $\mathbf{y}$ . This situation produces an image  $\mathbf{p}$  of the point  $\mathbf{x}$  in the correct position, but, because  $K_{1,2}$  is an off-diagonal term, the strength of the image may be incorrect at such a location.

**The term  $K_{1,3}$ .**

The phase of  $K_{1,3}$  is

$$\begin{aligned}\phi_{1,3}(\omega, \mathbf{y}, \mathbf{y}', \mathbf{p}, \mathbf{x}) &= \omega(\tau_3(\mathbf{y}, \mathbf{y}', \mathbf{x}) - \tau_1(\mathbf{y}, \mathbf{y}', \mathbf{p})) \\ &= \omega[ (|\mathbf{y} - \mathbf{x}| + |\mathbf{x} - \mathbf{z}| + |\mathbf{z} - \mathbf{y}'|) - (|\mathbf{y} - \mathbf{p}| + |\mathbf{p} - \mathbf{y}'|) ]\end{aligned}\quad (3.37)$$

Arguments similar to those for  $K_{1,2}$  show that the only critical point occurs in the case when  $\mathbf{x}$  is directly behind  $\mathbf{z}$  as seen from  $\mathbf{y}'$ ; in this case, the point  $\mathbf{p} = \mathbf{x}$  is a critical point. Again the image of such a point appears in the correct location, but its strength may be incorrect.

**The term  $K_{1,4}$ .**

The phase of  $K_{1,4}$  is

$$\begin{aligned}\phi_{1,4}(\omega, \mathbf{y}, \mathbf{y}', \mathbf{p}, \mathbf{x}) &= \omega(\tau_4(\mathbf{y}, \mathbf{y}', \mathbf{x}) - \tau_1(\mathbf{y}, \mathbf{y}', \mathbf{p})) \\ &= \omega[ (|\mathbf{y} - \mathbf{z}| + |\mathbf{z} - \mathbf{x}| + |\mathbf{x} - \mathbf{z}| + |\mathbf{z} - \mathbf{y}'|) - (|\mathbf{y} - \mathbf{p}| + |\mathbf{p} - \mathbf{y}'|) ]\end{aligned}\quad (3.38)$$

The stationary points satisfy

$$\begin{aligned}0 = \partial_\omega \phi_{1,4} &= (|\mathbf{y} - \mathbf{z}| + |\mathbf{z} - \mathbf{x}| + |\mathbf{x} - \mathbf{z}| + |\mathbf{z} - \mathbf{y}'|) - (|\mathbf{y} - \mathbf{p}| + |\mathbf{p} - \mathbf{y}'|) \\ 0 = \partial_{\mathbf{y}} \phi_{1,4} &= \widehat{(\mathbf{y} - \mathbf{z})} - \widehat{(\mathbf{y} - \mathbf{p})} \\ 0 = \partial_{\mathbf{y}'} \phi_{1,4} &= \widehat{(\mathbf{z} - \mathbf{y}')} - \widehat{(\mathbf{p} - \mathbf{y}')} \end{aligned}\quad (3.39)$$

The last two conditions of (3.39) say that  $\mathbf{p}$  must lie on the lines joining  $\mathbf{y}$  to  $\mathbf{z}$  and  $\mathbf{y}'$  to  $\mathbf{z}$ . Unless  $\mathbf{y} = \mathbf{y}'$ , this implies that  $\mathbf{p} = \mathbf{z}$ ; the first condition of (3.39) can then be satisfied only if  $\mathbf{x} = \mathbf{z}$ . In other words, this term can produce an artifact at the location of the foreground scatterer, which is not a location in which we are interested.

**The term  $K_{2,1}$ .**

The phase of  $K_{2,1}$  is the phase of  $K_{1,2}$  with  $\mathbf{y}$  and  $\mathbf{y}'$  interchanged.

**The term  $K_{2,2}$ .**

The phase of  $K_{2,2}$  is

$$\begin{aligned}\phi_{2,2}(\omega, \mathbf{y}, \mathbf{y}', \mathbf{p}, \mathbf{x}) &= \omega(\tau_2(\mathbf{y}, \mathbf{y}', \mathbf{x}) - \tau_2(\mathbf{y}, \mathbf{y}', \mathbf{p})) \\ &= \omega[(|\mathbf{y} - \mathbf{z}| + |\mathbf{z} - \mathbf{x}| + |\mathbf{x} - \mathbf{y}'|) - (|\mathbf{y} - \mathbf{z}| + |\mathbf{z} - \mathbf{p}| + |\mathbf{p} - \mathbf{y}'|)]\end{aligned}\quad (3.40)$$

The stationary points satisfy

$$\begin{aligned}0 = \partial_\omega \phi_{2,2} &= (|\mathbf{y} - \mathbf{z}| + |\mathbf{z} - \mathbf{x}| + |\mathbf{x} - \mathbf{y}'|) - (|\mathbf{y} - \mathbf{z}| + |\mathbf{z} - \mathbf{p}| + |\mathbf{p} - \mathbf{y}'|) \\ 0 = \partial_{\mathbf{y}} \phi_{2,2} &= \widehat{(\mathbf{y} - \mathbf{z})} - \widehat{(\mathbf{y} - \mathbf{z})} \\ 0 = \partial_{\mathbf{y}'} \phi_{2,2} &= \widehat{(\mathbf{x} - \mathbf{y}')} - \widehat{(\mathbf{p} - \mathbf{y}')} \end{aligned}\quad (3.41)$$

The second condition of (3.41) is vacuous; the third condition says that  $\mathbf{p}$  lies on the line joining  $\mathbf{y}'$  with  $\mathbf{x}$ . The first condition (in which the term  $|\mathbf{y} - \mathbf{z}|$  cancels) says that  $\mathbf{p}$  must lie on the same ellipsoid as  $\mathbf{x}$ . The only such point is  $\mathbf{p} = \mathbf{x}$ .

**The term  $K_{2,3}$ .**

The phase of  $K_{2,3}$  is

$$\begin{aligned}\phi_{2,3}(\omega, \mathbf{y}, \mathbf{y}', \mathbf{p}, \mathbf{x}) &= \omega(\tau_3(\mathbf{y}, \mathbf{y}', \mathbf{x}) - \tau_2(\mathbf{y}, \mathbf{y}', \mathbf{p})) \\ &= \omega[(|\mathbf{y} - \mathbf{x}| + |\mathbf{x} - \mathbf{z}| + |\mathbf{z} - \mathbf{y}'|) - (|\mathbf{y} - \mathbf{z}| + |\mathbf{z} - \mathbf{p}| + |\mathbf{p} - \mathbf{y}'|)]\end{aligned}\quad (3.42)$$

The stationary points satisfy

$$\begin{aligned}0 = \partial_\omega \phi_{2,3} &= (|\mathbf{y} - \mathbf{x}| + |\mathbf{x} - \mathbf{z}| + |\mathbf{z} - \mathbf{y}'|) - (|\mathbf{y} - \mathbf{z}| + |\mathbf{z} - \mathbf{p}| + |\mathbf{p} - \mathbf{y}'|) \\ 0 = \partial_{\mathbf{y}} \phi_{2,3} &= \widehat{(\mathbf{y} - \mathbf{x})} - \widehat{(\mathbf{y} - \mathbf{z})} \\ 0 = \partial_{\mathbf{y}'} \phi_{2,3} &= \widehat{(\mathbf{z} - \mathbf{y}')} - \widehat{(\mathbf{p} - \mathbf{y}')} \end{aligned}\quad (3.43)$$

The second equation of (3.43) says that  $\mathbf{x}$  lies directly behind  $\mathbf{z}$  when viewed from  $\mathbf{y}$ ; this implies that  $|\mathbf{x} - \mathbf{y}| - |\mathbf{y} - \mathbf{z}| = |\mathbf{z} - \mathbf{x}|$ ; similarly the third equation of (3.43) says that  $\mathbf{p}$  lies directly behind  $\mathbf{z}$  when viewed from  $\mathbf{y}'$ , which implies that  $|\mathbf{z} - \mathbf{y}'| - |\mathbf{p} - \mathbf{y}'| = -|\mathbf{z} - \mathbf{p}|$ . Thus the second and third equations of (3.43) imply that the first equation reduces to

$$2|\mathbf{z} - \mathbf{x}| = 2|\mathbf{z} - \mathbf{p}|. \quad (3.44)$$

This means that points  $\mathbf{x}$  lying along the line joining  $\mathbf{y}$  and  $\mathbf{z}$  can produce artifacts along the line joining  $\mathbf{y}'$  and  $\mathbf{z}$ . The artifact at  $\mathbf{p}$  is at the same distance from  $\mathbf{z}$  as the scatterer at  $\mathbf{x}$ .

**The term  $K_{2,4}$ .**

The phase of  $K_{2,4}$  is

$$\begin{aligned}\phi_{2,4}(\omega, \mathbf{y}, \mathbf{y}', \mathbf{p}, \mathbf{x}) &= \omega(\tau_4(\mathbf{y}, \mathbf{y}', \mathbf{x}) - \tau_2(\mathbf{y}, \mathbf{y}', \mathbf{p})) \\ &= \omega[(|\mathbf{y} - \mathbf{z}| + |\mathbf{z} - \mathbf{x}| + |\mathbf{x} - \mathbf{z}| + |\mathbf{z} - \mathbf{y}'|) - (|\mathbf{y} - \mathbf{z}| + |\mathbf{z} - \mathbf{p}| + |\mathbf{p} - \mathbf{y}'|)]\end{aligned}\quad (3.45)$$

The stationary points satisfy

$$\begin{aligned}0 = \partial_\omega \phi_{2,4} &= (|\mathbf{y} - \mathbf{z}| + |\mathbf{z} - \mathbf{x}| + |\mathbf{x} - \mathbf{z}| + |\mathbf{z} - \mathbf{y}'|) \\ &\quad - (|\mathbf{y} - \mathbf{z}| + |\mathbf{z} - \mathbf{p}| + |\mathbf{p} - \mathbf{y}'|) \\ 0 = \partial_{\mathbf{y}} \phi_{2,4} &= \widehat{(\mathbf{y} - \mathbf{z})} - \widehat{(\mathbf{y} - \mathbf{z})} \\ 0 = \partial_{\mathbf{y}'} \phi_{2,4} &= \widehat{(\mathbf{z} - \mathbf{y}')} - \widehat{(\mathbf{p} - \mathbf{y}')} \end{aligned}\quad (3.46)$$

The last equation of (3.46) says that  $\mathbf{p}$  lies directly behind  $\mathbf{z}$  when viewed from  $\mathbf{y}'$ . For such a point, we have  $|\mathbf{z} - \mathbf{y}'| - |\mathbf{p} - \mathbf{y}'| = -|\mathbf{z} - \mathbf{p}|$ , which converts the first equation of (3.46) into

$$2|\mathbf{x} - \mathbf{z}| = 2|\mathbf{z} - \mathbf{p}| \quad (3.47)$$

Thus every scatterer  $\mathbf{x}$  produces an artifact lying directly behind  $\mathbf{z}$  when seen from  $\mathbf{y}'$ . This artifact is at the same distance from  $\mathbf{z}$  as is  $\mathbf{x}$ .

**The term  $K_{3,1}$ .**

The phase of  $K_{3,1}$  is

$$\begin{aligned}\phi_{3,1}(\omega, \mathbf{y}, \mathbf{y}', \mathbf{p}, \mathbf{x}) &= \omega(\tau_1(\mathbf{y}, \mathbf{y}', \mathbf{x}) - \tau_3(\mathbf{y}, \mathbf{y}', \mathbf{p})) \\ &= \omega[(|\mathbf{y} - \mathbf{x}| + |\mathbf{x} - \mathbf{y}'|) - (|\mathbf{y} - \mathbf{p}|) - (|\mathbf{p} - \mathbf{z}| + |\mathbf{z} - \mathbf{y}'|)]\end{aligned}\quad (3.48)$$

This is the negative of the phase of  $K_{1,3}$  with  $\mathbf{x}$  and  $\mathbf{p}$  interchanged. Again the strength of scatterers directly behind  $\mathbf{z}$  can be incorrectly reconstructed.

**The term  $K_{3,2}$ .**

The phase of  $K_{3,2}$  is

$$\begin{aligned}\phi_{3,2}(\omega, \mathbf{y}, \mathbf{y}', \mathbf{p}, \mathbf{x}) &= \omega(\tau_2(\mathbf{y}, \mathbf{y}', \mathbf{x}) - \tau_3(\mathbf{y}, \mathbf{y}', \mathbf{p})) \\ &= \omega[(|\mathbf{y} - \mathbf{z}| + |\mathbf{z} - \mathbf{x}| + |\mathbf{x} - \mathbf{y}'|) \\ &\quad - (|\mathbf{y} - \mathbf{p}|) - (|\mathbf{p} - \mathbf{z}| + |\mathbf{z} - \mathbf{y}'|)]\end{aligned}\quad (3.49)$$

Again this is the negative of the phase of  $K_{2,3}$  with  $\mathbf{x}$  and  $\mathbf{p}$  interchanged; this term can cause scatters lying behind  $\mathbf{z}$  from  $\mathbf{y}$  to appear behind  $\mathbf{z}$  when viewed from  $\mathbf{y}'$ .

**The term  $K_{3,3}$ .**

The phase of  $K_{3,3}$  is

$$\begin{aligned}\phi_{3,3}(\omega, \mathbf{y}, \mathbf{y}', \mathbf{p}, \mathbf{x}) &= \omega(\tau_3(\mathbf{y}, \mathbf{y}', \mathbf{x}) - \tau_3(\mathbf{y}, \mathbf{y}', \mathbf{p})) \\ &= \omega[ (|\mathbf{y} - \mathbf{x}| + |\mathbf{x} - \mathbf{z}| + |\mathbf{z} - \mathbf{y}'|) \\ &\quad - (|\mathbf{y} - \mathbf{p}| + |\mathbf{p} - \mathbf{z}| + |\mathbf{z} - \mathbf{y}'|)]\end{aligned}\quad (3.50)$$

The stationary points satisfy

$$\begin{aligned}0 = \partial_\omega \phi_{3,3} &= (|\mathbf{y} - \mathbf{x}| + |\mathbf{x} - \mathbf{z}| + |\mathbf{z} - \mathbf{y}'|) \\ &\quad - (|\mathbf{y} - \mathbf{p}| + |\mathbf{p} - \mathbf{z}| + |\mathbf{z} - \mathbf{y}'|) \\ 0 = \partial_{\mathbf{y}} \phi_{3,3} &= \widehat{(\mathbf{y} - \mathbf{x})} - \widehat{(\mathbf{y} - \mathbf{p})} \\ 0 = \partial_{\mathbf{y}'} \phi_{3,3} &= \widehat{(\mathbf{z} - \mathbf{y}')} - \widehat{(\mathbf{z} - \mathbf{y}')} \end{aligned}\quad (3.51)$$

In the first equation of (3.51), the term  $|\mathbf{z} - \mathbf{y}'|$  cancels; we see that  $\mathbf{p}$  must lie on the same ellipsoid as  $\mathbf{x}$  and must lie in the same direction as  $\mathbf{x}$  from  $\mathbf{y}$ . The only such point is  $\mathbf{p} = \mathbf{x}$ .

**The term  $K_{3,4}$ .**

The phase of  $K_{3,4}$  is

$$\begin{aligned}\phi_{3,4}(\omega, \mathbf{y}, \mathbf{y}', \mathbf{p}, \mathbf{x}) &= \omega(\tau_4(\mathbf{y}, \mathbf{y}', \mathbf{x}) - \tau_3(\mathbf{y}, \mathbf{y}', \mathbf{p})) \\ &= \omega[ (|\mathbf{y} - \mathbf{z}| + 2|\mathbf{x} - \mathbf{z}| + |\mathbf{z} - \mathbf{y}'|) \\ &\quad - (|\mathbf{y} - \mathbf{p}| + |\mathbf{p} - \mathbf{z}| + |\mathbf{z} - \mathbf{y}'|)]\end{aligned}\quad (3.52)$$

The stationary points satisfy

$$\begin{aligned}0 = \partial_\omega \phi_{3,4} &= (|\mathbf{y} - \mathbf{z}| + 2|\mathbf{x} - \mathbf{z}| + |\mathbf{z} - \mathbf{y}'|) - (|\mathbf{y} - \mathbf{p}| + |\mathbf{p} - \mathbf{z}| + |\mathbf{z} - \mathbf{y}'|) \\ 0 = \partial_{\mathbf{y}} \phi_{3,4} &= \widehat{(\mathbf{y} - \mathbf{z})} - \widehat{(\mathbf{y} - \mathbf{p})} \\ 0 = \partial_{\mathbf{y}'} \phi_{3,4} &= \widehat{(\mathbf{z} - \mathbf{y}')} - \widehat{(\mathbf{z} - \mathbf{y}')} \end{aligned}\quad (3.53)$$

From the second equation of (3.53), we see that  $\mathbf{y}$ ,  $\mathbf{z}$ , and  $\mathbf{p}$  all lie on the same line, which implies that  $|\mathbf{y} - \mathbf{z}| - |\mathbf{y} - \mathbf{p}| = -|\mathbf{z} - \mathbf{p}|$ . The first equation of (3.53) then reduces to  $2|\mathbf{x} - \mathbf{z}| = 2|\mathbf{p} - \mathbf{z}|$ .

Thus we see that this term can give rise to artifacts directly behind  $\mathbf{z}$  as viewed from  $\mathbf{y}$ .

**The term  $K_{4,4}$ .**

$$\begin{aligned}\phi_{4,4}(\omega, \mathbf{y}, \mathbf{y}', \mathbf{p}, \mathbf{x}) &= \omega(\tau_4(\mathbf{y}, \mathbf{y}', \mathbf{x}) - \tau_4(\mathbf{y}, \mathbf{y}', \mathbf{p})) \\ &= \omega[ (|\mathbf{y} - \mathbf{z}| + 2|\mathbf{z} - \mathbf{x}| + |\mathbf{z} - \mathbf{y}'|) \\ &\quad - (|\mathbf{y} - \mathbf{z}| + 2|\mathbf{z} - \mathbf{p}| + |\mathbf{z} - \mathbf{y}'|)]\end{aligned}$$

$$-((|\mathbf{y} - \mathbf{z}| + 2|\mathbf{z} - \mathbf{p}| + |\mathbf{z} - \mathbf{y}'|))) \quad (3.54)$$

The stationary points satisfy

$$\begin{aligned} 0 = \partial_{\omega} \phi_{4,4} &= ((|\mathbf{y} - \mathbf{z}| + |\mathbf{z} - \mathbf{x}| + |\mathbf{x} - \mathbf{z}| + |\mathbf{z} - \mathbf{y}'|) \\ &\quad - (|\mathbf{y} - \mathbf{z}| + |\mathbf{z} - \mathbf{p}| + |\mathbf{p} - \mathbf{z}| + |\mathbf{z} - \mathbf{y}'|)) \\ 0 = \partial_{\mathbf{y}} \phi_{4,4} &= (\widehat{\mathbf{y} - \mathbf{z}}) - (\widehat{\mathbf{y} - \mathbf{z}}) \\ 0 = \partial_{\mathbf{y}'} \phi_{4,4} &= (\widehat{\mathbf{z} - \mathbf{y}'}) - (\widehat{\mathbf{z} - \mathbf{y}'}) \end{aligned} \quad (3.55)$$

The last two equations of (3.55) are vacuous; the first equation reduces to  $|\mathbf{x} - \mathbf{z}| = |\mathbf{p} - \mathbf{z}|$ , which says merely that  $\mathbf{p}$  must lie on the same travel-time sphere about  $\mathbf{z}$  as does  $\mathbf{x}$ . In other words, backprojection of a path in which both the incident and scattered wave bounce off of  $\mathbf{z}$  cannot be used to determine the location of a scatterer at  $\mathbf{x}$ . This is because the scatterer at  $\mathbf{z}$  is isotropic: after a wave scatters from a point scatterer, it loses all information about the direction from which it came. In the image, this term causes spherical artifacts around  $\mathbf{z}$ ; consequently we omit the term  $B_4$  from our imaging operator, and we do not consider terms of the form  $K_{4,j}$ .

### Determination of the $b_i$

We have found that the imaging operator should be composed of three terms:

$$I(\mathbf{p}) = \sum_{i=1}^3 B_i[g^{\text{sc}}](\mathbf{p}) \approx \sum_{i=1}^3 \sum_{j=1}^4 \int K_{i,j}(\mathbf{p}, \mathbf{x}) q(\mathbf{x}) d\mathbf{x} \quad (3.56)$$

and that moreover, if we restrict our attention to the target region (avoiding regions behind the scatterer at  $\mathbf{z}$ ), only the diagonal terms  $K_{i,i}$  contribute (to leading order) to the image. We have shown above that this imaging operator correctly positions scatterers in the target region.

Next we turn our attention to the scatterers' strengths, which are controlled by the factors  $b_i$  appearing in  $B_i$ . To determine the  $b_i$ , we attempt to transform each  $K_{i,i}$  into a delta function. We recall that a delta function can be written as an oscillatory integral in the form  $\delta(\mathbf{p} - \mathbf{x}) = (2\pi)^{-3} \int \exp[i(\mathbf{p} - \mathbf{x}) \cdot \boldsymbol{\xi}] d\boldsymbol{\xi}$ . Since  $\mathbf{p}$  and  $\mathbf{x}$  are three-dimensional, we are trying to express  $K_{i,i}$  as a three-dimensional integral. This means that our measured data should depend at least three variables. This would be the case, for example, for data from a single array antenna, where the data depends on  $t$  and two array coordinates  $\mathbf{y}$ . If more data is available, for example in the case in which we have a separate transmitting and receiving arrays, we carry out the analysis below for a three-dimensional subset of the data (say,  $t$  and the transmitter coordinates  $\mathbf{y}$ ) and then simply integrate over the remaining variables.

In the exponent of (3.31), we use the identity

$$f(\mathbf{x}) - f(\mathbf{p}) = \int_0^1 \frac{d}{d\lambda} f(\mathbf{p} + \lambda(\mathbf{x} - \mathbf{p})) d\lambda = (\mathbf{x} - \mathbf{p}) \cdot \int_0^1 (\nabla f)(\mathbf{p} + \lambda(\mathbf{x} - \mathbf{p})) d\lambda \quad (3.57)$$



to write

$$\omega[\tau_i(\mathbf{y}, \mathbf{y}', \mathbf{x}) - \tau_i(\mathbf{y}, \mathbf{y}', \mathbf{p})] = (\mathbf{x} - \mathbf{p}) \cdot \Xi^i(\mathbf{p}, \mathbf{x}, \mathbf{y}, \mathbf{y}', \omega); \quad (3.58)$$

explicitly, the  $\Xi^i$  are given by

$$\Xi^i(\mathbf{p}, \mathbf{x}, \mathbf{y}, \mathbf{y}', \omega) = \omega \int_0^1 \nabla_{\mathbf{x}'} \tau_i(\mathbf{y}, \mathbf{y}', \mathbf{x}') \Big|_{\mathbf{x}' = \mathbf{p} + \lambda(\mathbf{x} - \mathbf{p})} d\lambda. \quad (3.59)$$

When  $\mathbf{p} = \mathbf{x}$ , we have

$$\begin{aligned} \Xi^1(\mathbf{p}, \mathbf{p}, \mathbf{y}, \mathbf{y}', \omega) &= \omega [\widehat{\mathbf{p} - \mathbf{y}} + \widehat{\mathbf{p} - \mathbf{y}'}] \\ \Xi^2(\mathbf{p}, \mathbf{p}, \mathbf{y}, \mathbf{y}', \omega) &= \omega [\widehat{\mathbf{p} - \mathbf{y}} + \widehat{\mathbf{p} - \mathbf{z}}] \\ \Xi^3(\mathbf{p}, \mathbf{p}, \mathbf{y}, \mathbf{y}', \omega) &= \omega [\widehat{\mathbf{p} - \mathbf{z}} + \widehat{\mathbf{p} - \mathbf{y}'}] \end{aligned} \quad (3.60)$$

In the integral (3.31) for  $K_{1,1}$  and  $K_{2,2}$ , we make the change of variables

$$(\omega, \mathbf{y}) \rightarrow \boldsymbol{\xi}^i = \Xi^i(\mathbf{p}, \mathbf{p}, \mathbf{y}, \mathbf{y}', \omega); \quad (3.61)$$

in  $K_{3,3}$  we make the change of variables

$$(\omega, \mathbf{y}') \rightarrow \boldsymbol{\xi}^i = \Xi^3(\mathbf{p}, \mathbf{p}, \mathbf{y}, \mathbf{y}', \omega); \quad (3.62)$$

This transforms the expression (3.31) for  $K_{1,1}$  and  $K_{2,2}$  into

$$\begin{aligned} K_{i,i}(\mathbf{p}, \mathbf{x}) &= 2\pi \int e^{i(\mathbf{p} - \mathbf{x}) \cdot \boldsymbol{\xi}^i} b_i(\omega, \mathbf{p}, \mathbf{y}, \mathbf{y}') a_i(\omega, \mathbf{y}, \mathbf{y}', \mathbf{x}) \\ &\quad \left| \det \left( \frac{\partial(\omega, \mathbf{y})}{\partial \boldsymbol{\xi}^i} \right) (\mathbf{p}, \mathbf{y}, \mathbf{y}', \omega) \right| d\boldsymbol{\xi}^i d\mathbf{y}' + E_i, \end{aligned} \quad (3.63)$$

where  $\mathbf{y} = \mathbf{y}(\boldsymbol{\xi})$  and  $\omega = \omega(\boldsymbol{\xi})$  and  $E_i$  denotes a smooth error term;  $K_{3,3}$  is transformed into a similar expression except that the integral is over  $\mathbf{y}$  instead of  $\mathbf{y}'$ .

Equation (3.63) exhibits the point spread function  $K$  as the kernel of a pseudodifferential operator. Pseudodifferential operators have the *pseudolocal* property [44], i.e., they do not move singularities or change their orientation. It is immediately clear from (3.63) that provided the Jacobian  $|\partial(\omega, \mathbf{y})/\partial \boldsymbol{\xi}^i|$  is nonzero, the leading order contribution to the image comes from the points  $\mathbf{p} = \mathbf{x}$ .

We see from (3.63) that the backprojection weighting function  $b$  should be chosen as

$$b_i(\omega, \mathbf{p}, \mathbf{y}, \mathbf{y}') = \frac{\left| \left( \frac{\partial \boldsymbol{\xi}^i}{\partial(\omega, \mathbf{y})} \right) (\mathbf{p}, \mathbf{y}, \mathbf{y}', \omega) \right| \chi_i(\mathbf{p}, \mathbf{y}, \mathbf{y}', \omega)}{(2\pi) a_i(\omega, \mathbf{y}, \mathbf{y}', \mathbf{p})} \quad (3.64)$$

where  $\chi_i$  is a smooth cutoff function that prevents division by zero in (3.64) and that is chosen so that

$$\chi_1[\mathbf{p}, \mathbf{y}(\boldsymbol{\xi}), \mathbf{y}', \omega(\boldsymbol{\xi})] + \chi_2[\mathbf{p}, \mathbf{y}(\boldsymbol{\xi}), \mathbf{y}', \omega(\boldsymbol{\xi})] + \chi_3[\mathbf{p}, \mathbf{y}, \mathbf{y}'(\boldsymbol{\xi}), \omega(\boldsymbol{\xi})] = \frac{1}{(2\pi)^3} \quad (3.65)$$

in as large a region of  $\xi$ -space (i.e.,  $(\omega, \mathbf{y})$ -space) as possible.

The Jacobian determinants  $|\partial(\omega, \mathbf{y})/\partial\xi^i|$  are called the *Beylkin determinants* [?] [8]. The first one is

$$\frac{\partial\xi^1}{\partial(\omega, \mathbf{y})} = \det \left( \widehat{\mathbf{p} - \mathbf{y}} + \widehat{\mathbf{p} - \mathbf{y}'} \quad -\omega P_{\widehat{\mathbf{p} - \mathbf{y}}} \mathbf{e}^1 \quad -\omega P_{\widehat{\mathbf{p} - \mathbf{y}}} \mathbf{e}^2 \right) \quad (3.66)$$

where  $P_{\mathbf{R}}$  is the projection operator that projects a vector onto the plane perpendicular to  $\hat{\mathbf{R}}$ :

$$P_{\mathbf{R}}\mathbf{v} = \frac{\mathbf{v} - \hat{\mathbf{R}}(\hat{\mathbf{R}} \cdot \mathbf{v})}{|\mathbf{R}|} \quad (3.67)$$

and where  $\mathbf{e}^1$  and  $\mathbf{e}^2$  denote unit vectors tangent to the receiving array antenna. Similarly,

$$\frac{\partial\xi^2}{\partial(\omega, \mathbf{y})} = \det \left( \widehat{\mathbf{p} - \mathbf{y}} + \widehat{\mathbf{p} - \mathbf{z}} \quad -\omega P_{\widehat{\mathbf{p} - \mathbf{y}}} \mathbf{e}^1 \quad -\omega P_{\widehat{\mathbf{p} - \mathbf{y}}} \mathbf{e}^2 \right) \quad (3.68)$$

$$\frac{\partial\xi^3}{\partial(\omega, \mathbf{y})} = \det \left( \widehat{\mathbf{p} - \mathbf{z}} + \widehat{\mathbf{p} - \mathbf{y}'} \quad -\omega P_{\widehat{\mathbf{p} - \mathbf{y}'}} \mathbf{e}'^1 \quad -\omega P_{\widehat{\mathbf{p} - \mathbf{y}'}} \mathbf{e}'^2 \right) \quad (3.69)$$

where  $\mathbf{e}'^1$  and  $\mathbf{e}'^2$  denote unit vectors tangent to the transmitting array.

The determinants of (3.66), (3.68), and (3.69) can be calculated easily. These determinants are nonzero because their column vectors are linearly independent: for example, the vector  $\widehat{\mathbf{p} - \mathbf{y}} + \widehat{\mathbf{p} - \mathbf{y}'}$  points from the antennas towards the target, whereas  $P_{\widehat{\mathbf{p} - \mathbf{y}}} \mathbf{e}^1$  and  $P_{\widehat{\mathbf{p} - \mathbf{y}}} \mathbf{e}^2$  are roughly tangent to the antenna array.

## Summary.

For the case of a single point scatterer in the foreground, the imaging operator should be

$$I(\mathbf{p}) = \sum_{j=1}^3 B_j[g^{\text{sc}}](\mathbf{p}) = \sum_{j=1}^3 \int e^{i\omega[t - \tau_j(\mathbf{y}, \mathbf{y}', \mathbf{p})]} b_j(\omega, \mathbf{p}, \mathbf{y}, \mathbf{y}') g^{\text{sc}}(t, \mathbf{y}, \mathbf{y}') dt d\mathbf{y} d\mathbf{y}' \quad (3.70)$$

where the  $\tau_j$  are given by (3.27), where the  $b_j$  are chosen as in (3.64), and where the Jacobian determinants are given by (3.66), (3.68), and (3.69). We note that imaging does *not* require a lot of bookkeeping in the sense that different operators do not need to be applied to different parts of the data. Formation of the imaging operator does, however, require knowledge of the foreground scatterer and does require that the backprojection be done only along round-trip paths that include a direct one-way path between antenna and target.

### 3.4 Resolution

With the  $b_i$  chosen as in (3.64),  $K$  is as close to a delta function as possible for the measurement geometry. The degree to which it approximates a delta function is determined by the support of  $\chi$ , which is in turn determined through (3.60) by the overall size of the measurement aperture.

For the case of a single point scatterer, we determine as follows the regions in  $\xi$ -space over which we have data. The resolution we obtain from  $K_{1,1}$  is determined by the region in Fourier space covered by  $\Xi^1$  as  $\mathbf{y}$  and  $\mathbf{y}'$  range over the antennas and as  $\omega$  varies over the bandwidth of the transmitted waveform. This region, which is determined by the first equation of (3.60), is sketched in Figure 3.2. The resolution region we obtain from  $K_{2,2}$  (sketched in Figure 3.3) is determined by the second equation of (3.60), and the resolution region obtained from  $K_{3,3}$  (Figure 3.4) is determined by the third equation of (3.60).

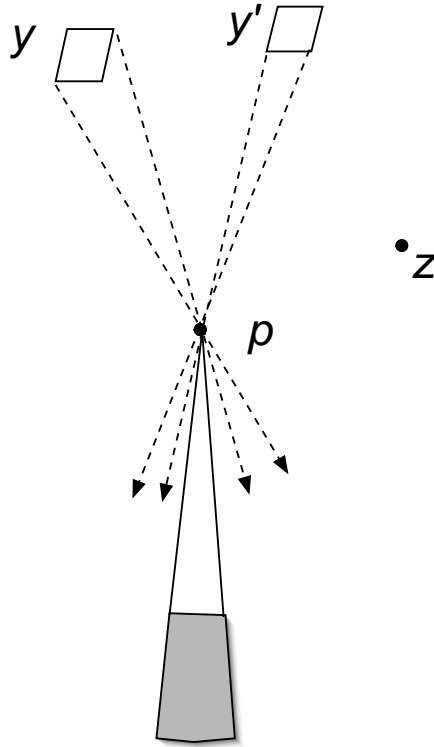


Figure 3.2: Region in Fourier space obtained from  $K_{1,1}$ .

### 3.5 Conclusions from the theoretical study

We have exhibited a backprojection imaging method that makes use of multipath scattering data from point scatterers assumed to be in the foreground of the target. We find that in order to avoid

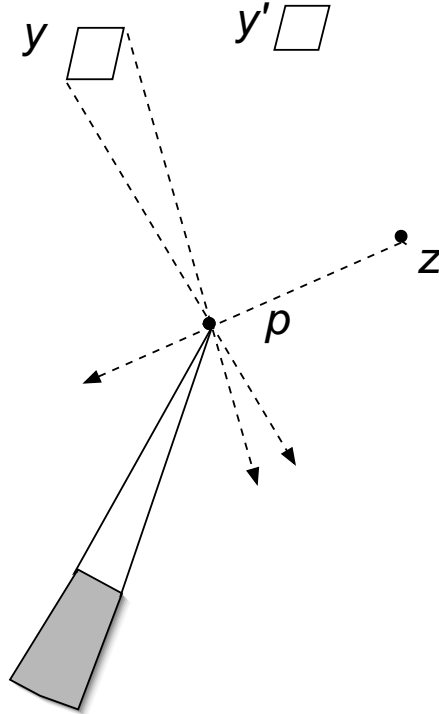


Figure 3.3: Region in Fourier space obtained from  $K_{2,2}$

artifacts, we must backproject only along those round-trip paths that involve a direct path from the target to the antenna. The use of such multipath scattering enhances the resolution obtained in the image.

## 3.6 Simulations

Much of this work has been joint work with Adam Bojanczyk.

The simulation work proceeded in four stages:

1. Simulations of the data from a single view
2. Reconstructions from simulated single-view data
3. Simulations of the data from multiple views
4. Reconstructions from simulated multiple-view data

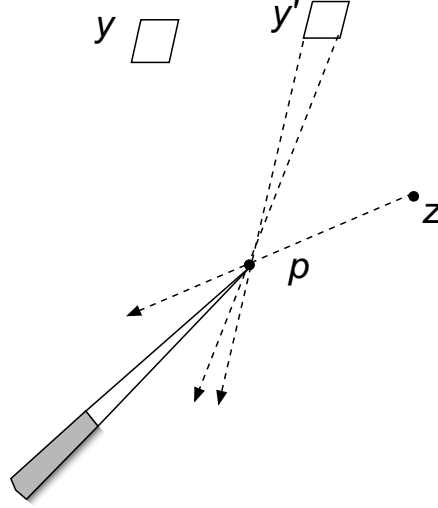


Figure 3.4: Region in Fourier space obtained from  $K_{3,3}$

### 3.6.1 Simulation of single-view data

For the simulations we used a frequency-domain formula for multiple scattering from point scatterers [11, 9]. The code allows for input of an arbitrary number of point scatterers located at arbitrary positions. The code produces stepped-frequency data for a frequency range that can be input by the user. This code produces backscattered data; i.e., the transmitter and receiver are assumed to coincide.

### 3.6.2 Reconstructions from a single view

We implemented a backprojection algorithm, which is flexible in that it can be used for arbitrary, sparse viewing locations. An input into the code is the location of one of the point scatterers; knowledge of this location is used in the multipath imaging part of the algorithm. The single-bounce backprojection from this known scatterer is subtracted out of the image.

The algorithm produces a backprojection from the single-bounce scattering and a backprojection from the double-bounce scattering. Of course, since the algorithm doesn't know which parts of the data come from which paths, the single-bounce backprojection contains artifacts due to the double-bounce paths, and vice versa.

We began with the case of two point scatterers. The reconstructions produced in this case are instructive. Figure 2 shows the image that would be produced by a standard backprojection algorithm that does not account for multipath scattering. Recall that the known scatterer has been subtracted out, so this is the view of the single unknown scatterer. We note that this image contains

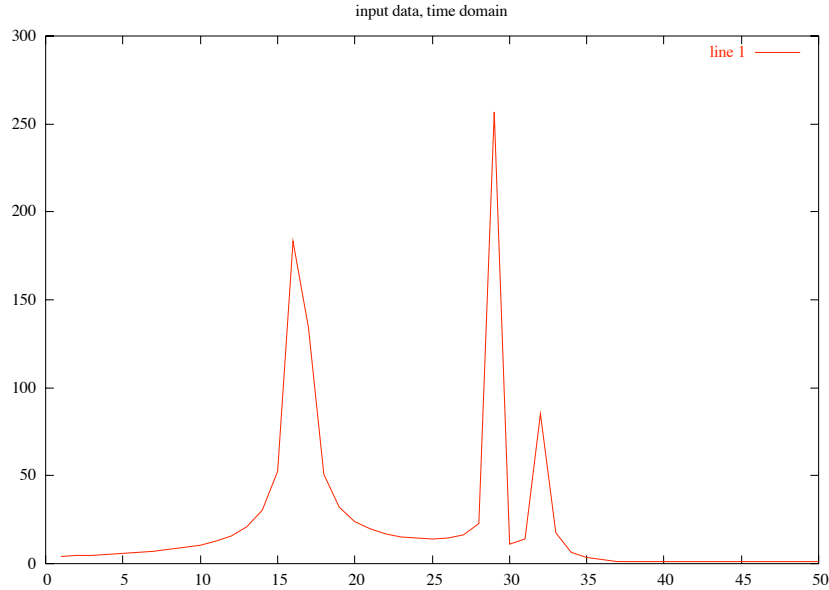


Figure 3.5: A time-domain plot of (the magnitude of) data from two point scatterers. The first two peaks are from direct scattering; the third peak is from the wave that bounces off one scatterer onto the second and then propagates back to the radar

no cross-range information about the scatterer location.

Figure 3 shows the double-bounce backprojected image. These curves are ellipses with one focus at the radar and the other focus at the position of the known scatterer.

Figure 4 shows the superposition of Figures 2 and 3. In this figure, we can find the cross-range location of the scatterer: it is at the intersection of the single-bounce and double-bounce curves. We note also artifacts that appear behind the known scatterer (as viewed from the radar position); this is predicted by the theory.

Backprojection of data from three point scatterers is much more complicated and is difficult to interpret. For this reason we went to a multiple-view scenario.

### 3.6.3 Simulation of multiple-view data

Simulation of multiple-view data was done by including rotation of the point scatterers. A range-angle plot of simulated data is shown in Figure 5. We see sine curves from each scatterer, together with the multiple-scattering curve on top (at a greater range). This simulation does NOT include attenuation from geometrical spreading.

We have run numerical experiments with the correct geometrical-spreading attenuation for three-dimensional point sources and scatterers; the amplitude variation then makes the curves more

difficult to see. To more closely simulate the experimental data from the range, probably the antennas can be modeled as point sources, but the pipes should be modeled as TWO-dimensional points, so that the geometrical spreading is  $r^{-1/2}$  rather than  $r^{-1}$ . This correction has not been incorporated into the code. In the present version of the code, attenuation corrections appropriate for point scatterers in three dimensions is present but was commented out to produce the figures in this report.

### 3.6.4 Multiple-view reconstruction

The single-bounce reconstruction is shown in Figure 3.10; the double-bounce reconstruction is shown in Figure 3.11, and the sum is shown in Figure 3.12. A horizontal slice through Figure 3.10 is compared with the corresponding slice through Figure ?? in Figure 3.13; this comparison shows the improvement obtainable by including the double-bounce backprojection.

These reconstructions are done from a subset of the data shown in Figure 3.9, which does not include attenuation from geometrical spreading. Including this attenuation is problematic: for well-separated point scatterers in three dimensions, the returns from more distant scatterers and the multiple-scattering returns are so weak that multiple-scattering artifacts are only barely visible in the single-bounce reconstructions. In other words, multipath artifacts are not problematic unless a) the scatterers are not well-separated, or b) the three-dimensional point scatterer assumption is not appropriate.

When attenuation due to geometrical spreading is included, and the strength of the double-bounce reconstruction is boosted sufficiently to be seen, this causes problems. In particular, boosting the strength of the double-bounce reconstruction means that the strength of the artifacts from single-bounce scattering are also automatically boosted. These artifacts tend to overshadow the desired image. Presumably these difficulties would be alleviated by using a broader bandwidth, so that the data more closely approximates the assumptions of the theory.

### 3.6.5 Work with data from the radar range

The first step was to plot the data. The (magnitude of) the data is shown as a range-angle plot in Figures 3.14 (3 pipes), 3.15 (1 pipe), and 3.16 (2 pipes). Clearly the 1- and 2-pipe data is much noisier than the 3-pipe data. All three datasets show scintillation, the interference effects from scatterers in the same or nearby range cells. This effect was much weaker in the simulated data above, because those examples are from scatterers well-separated in range.

The reconstructed image from the 3-pipe data, using single-bounce backprojection only, is shown in Figure 8. The two closer scatterers are seen clearly, but the third scatterer is obscured by multipath scattering artifacts. This reconstruction is comparable to the one produced by Justin Bracken's code, but is done by backprojection rather than a Fourier transform.

A double-bounce backprojection has not yet been successful, because I have not yet succeeded in finding the location of one of the scatterers and subtracting it out. I have obtained an estimate of the location of the strongest scatterer, but subtracting out a point scatterer at that location does not remove it. This may be because the strongest scatterer was a pipe sufficiently large that it is not behaving as a point scatterer.

### 3.6.6 Issues for the future

The following issues remain.

1. Put in the correct geometrical spreading factors into the data simulator and into the reconstruction codes.
2. Determine whether increasing the bandwidth mitigates the single-bounce artifacts in the double-bounce reconstruction. The theory predicts that for sufficiently wide bandwidth, singularities (points and edges) will be reconstructed at the correct positions, and the rest of the image (the artifacts) will be smoother. How wide must the bandwidth be in order to see these effects?
3. Simulated data for 3 point scatterers does not look like the experimental range data for 3 point scatterers – why? Is this only because good estimates for the pipe positions have not been put into the code? Or are the waves bouncing more than once? Is there a resonance phenomenon because the pipes are so closely spaced?
4. Write code for finding the positions of the closest point scatterers; incorporate this into the reconstruction code.
5. Figure out how to subtract the strongest scatterer if it is not point-like. It may be possible to treat it as a circular superposition of point-like scatterers, find its radius using an optimization approach, and subtract out an exact solution for a cylinder. A question then arises of its effect on the multiple scattering processes; will the multiple scattering from such a large object be sufficiently similar to that of a point that we can expect the theory to be applicable?
6. Address issues of noise in the 2-pipe data.
7. Explore alternative approaches for dealing with multiple scattering, such as for example using the exact solution for multiple scattering from point sources together with an optimization method to best fit the data.



## Acknowledgments

This work was also supported in part by AFOSR agreement number F49620-03-1-0051, by Rensselaer Polytechnic Institute, by the UCLA Institute for Pure and Applied Mathematics, by the NSF Focused Research Groups in the Mathematical Sciences program, and by CenSSIS, the Center for Subsurface Sensing and Imaging Systems, under the Engineering Research Centers Program of the National Science Foundation (award number EEC-9986821).

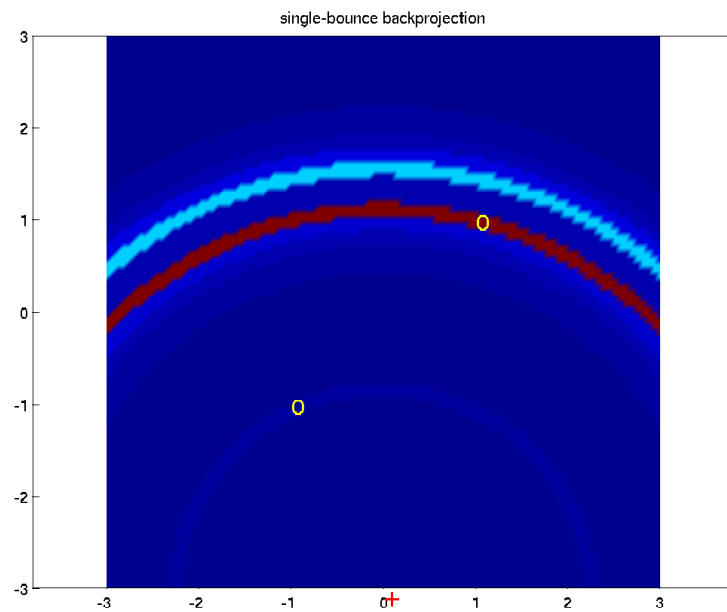


Figure 3.6: The single-bounce backprojected image of a point scatterer, with the true locations shown as yellow circles. The radar position is the red cross superimposed on the scale at the bottom. The multipath scattering appears as a second scatterer located farther away from the radar. Note that no cross-range information can be obtained from this single view.

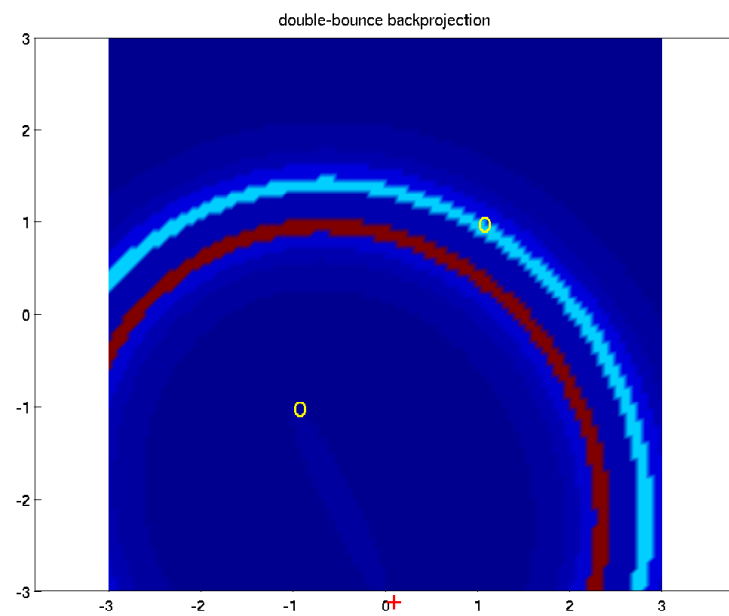


Figure 3.7: The double-bounce backprojected image from two point scatterers, with the true locations shown as yellow circles. In this image, the single-bounce scattering causes an artifact.

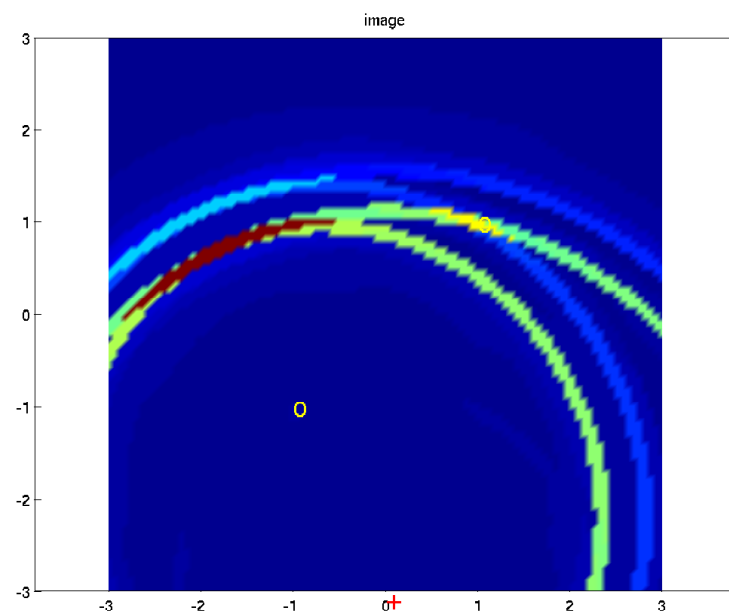


Figure 3.8: The backprojected image from two point scatterers; this is a superposition of Figures 2 and 3. The true locations are shown as yellow circles. See the text for discussion.

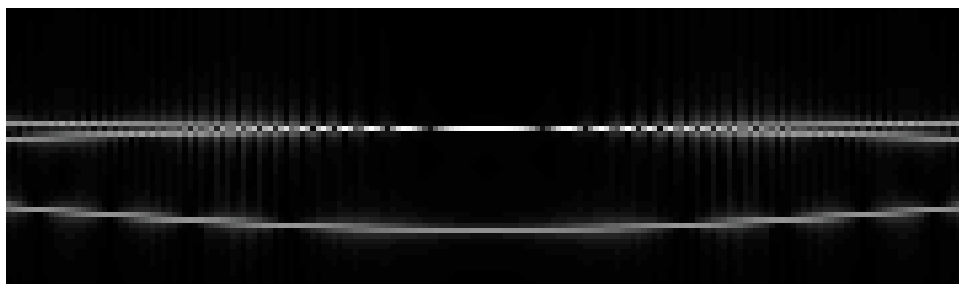


Figure 3.9: Range-angle plot of multiple-view data for two scatterers. Here views are taken every  $.5^\circ$  over angles from  $0$  to  $90^\circ$ .

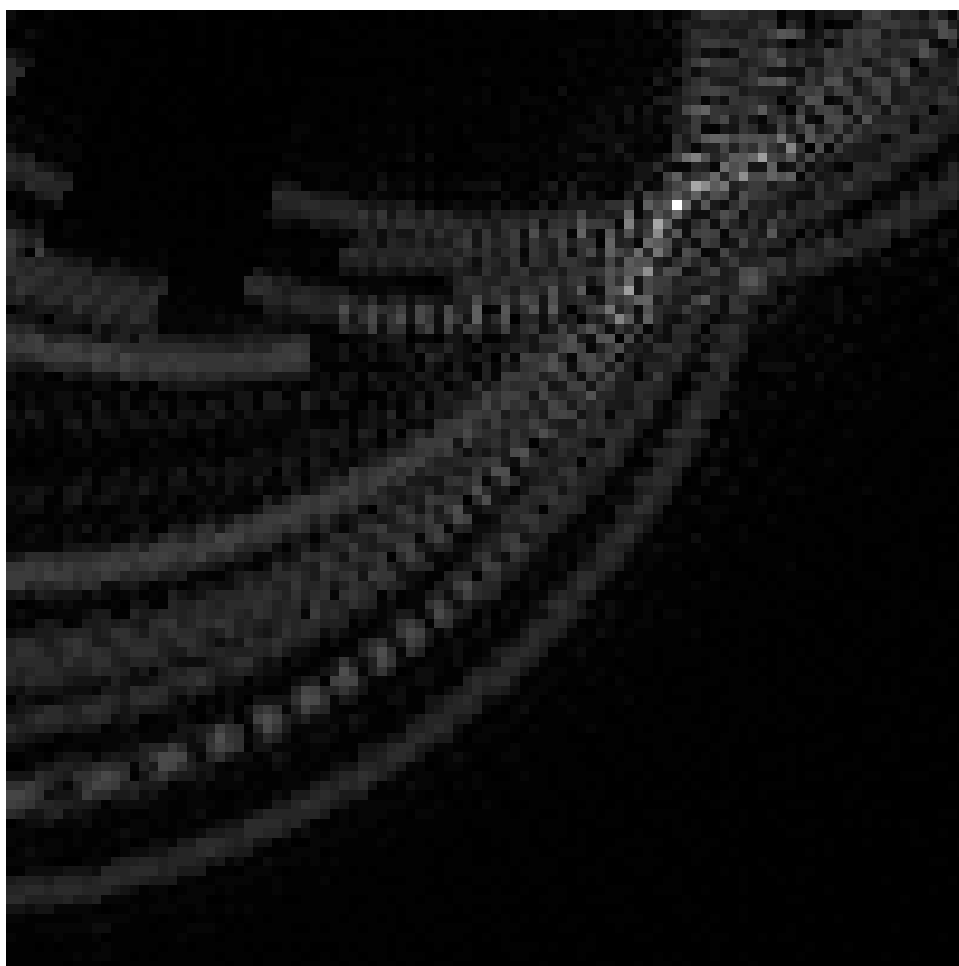


Figure 3.10: Single-bounce reconstruction from 10 views spanning  $90^\circ$  (each  $9^\circ$  apart). The radar starts from the top and moves to the left side.

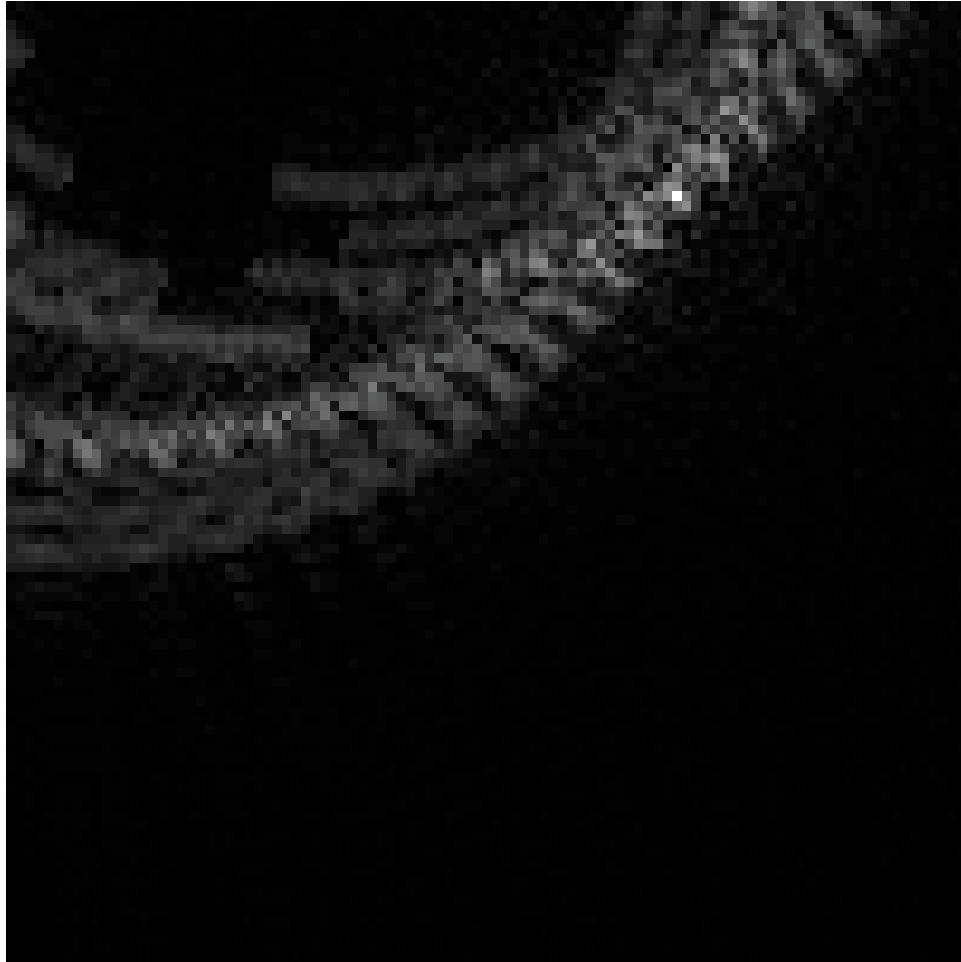


Figure 3.11: Double-bounce reconstruction from the same dataset as Figure 3.10.

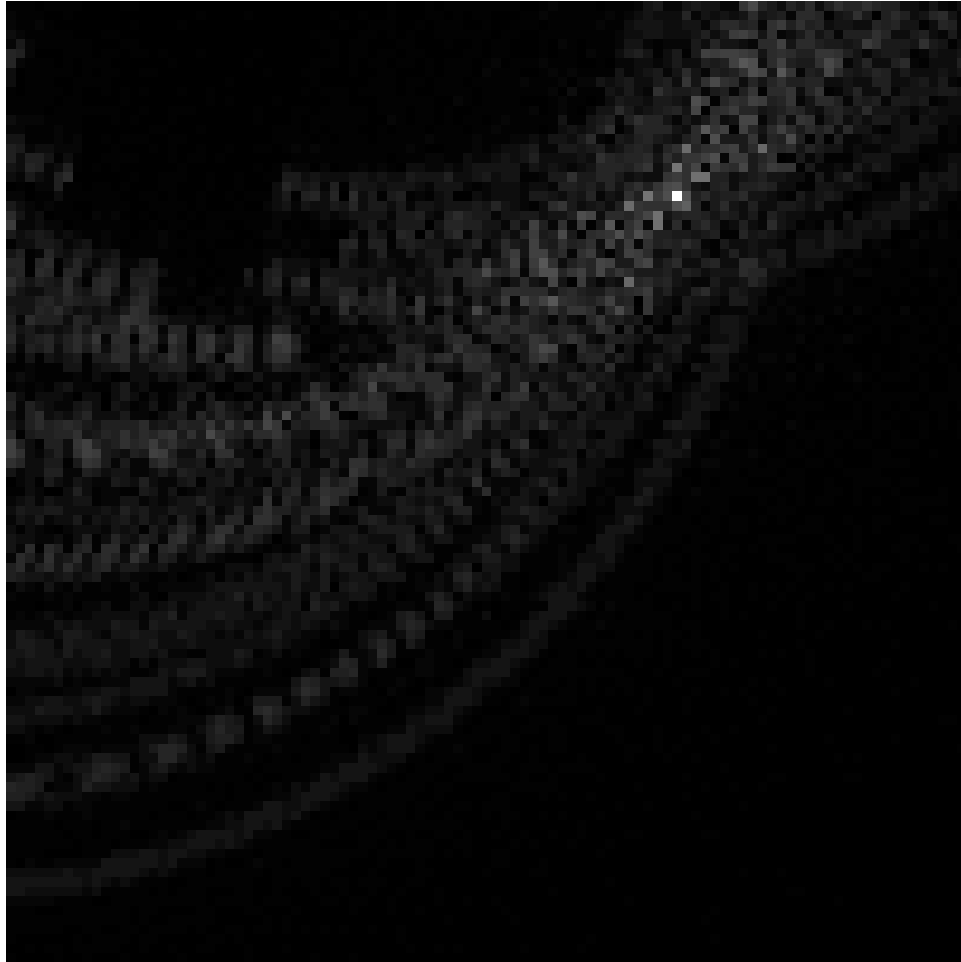


Figure 3.12: The sum of Figures 3.10 and 3.11 .

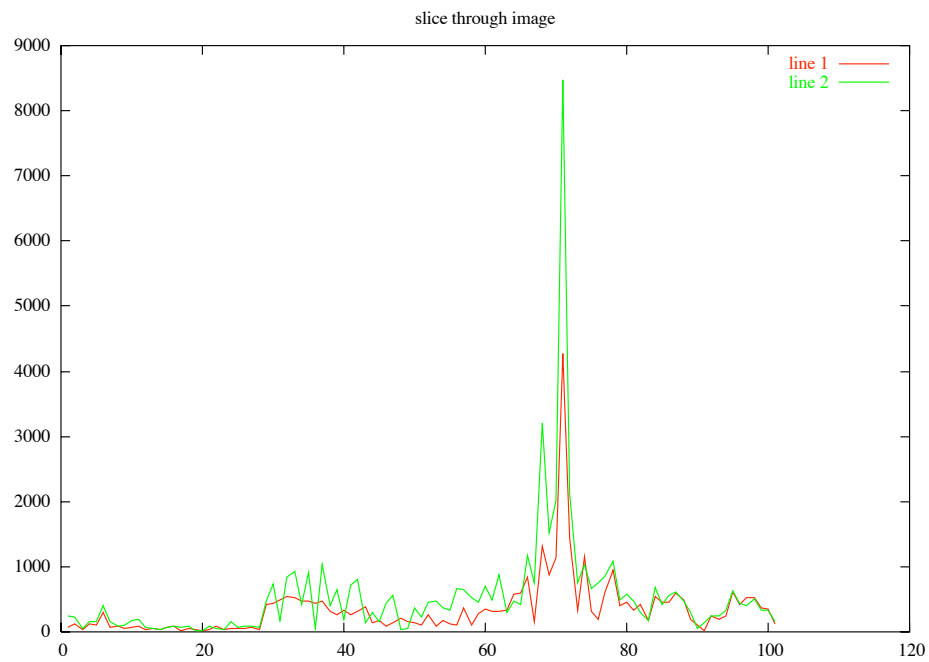


Figure 3.13: The red line is a horizontal slice through Figure 3.10 (the single-bounce backprojection); the green line is the same slice through Figure 3.12 (the sum of the single-bounce and double-bounce backprojections). This shows the improvement from adding the double-bounce backprojection.



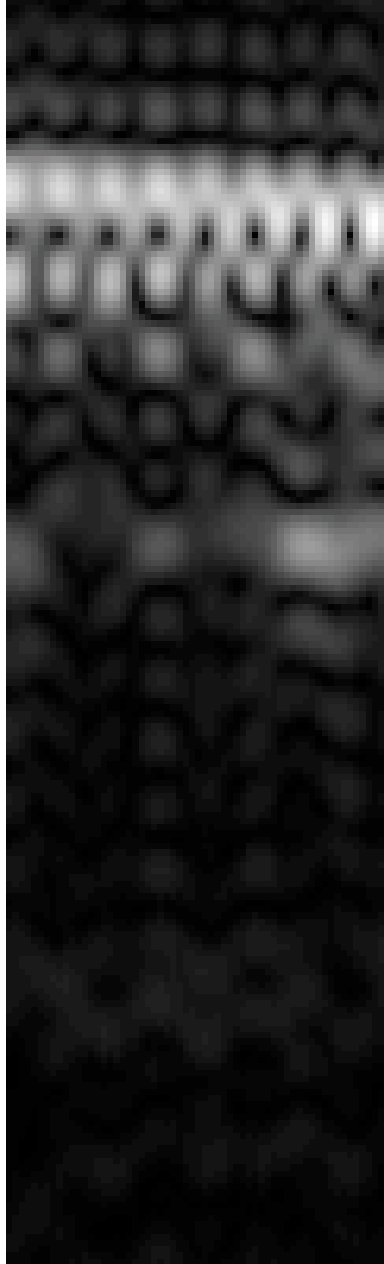


Figure 3.14: Range-angle plot of the (magnitude of) the experimental data from 3 pipes.

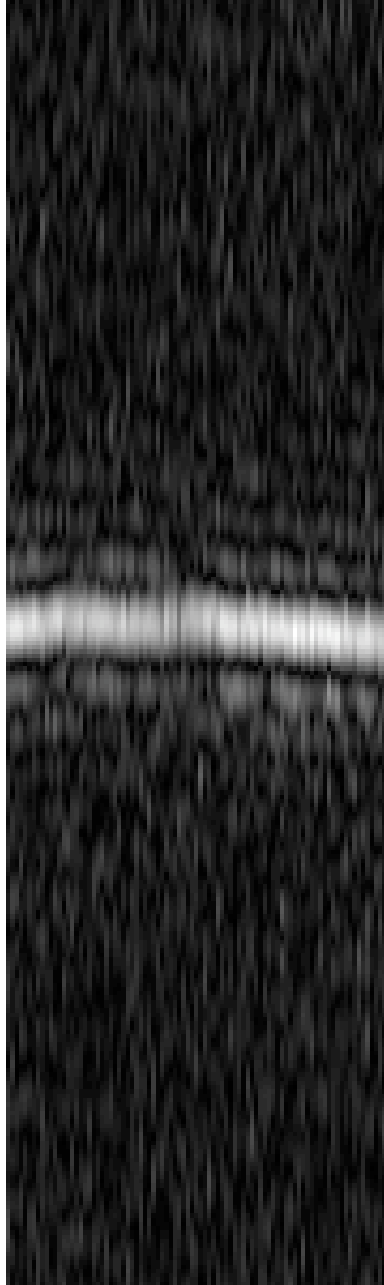


Figure 3.15: Range-angle plot of the (magnitude of) the experimental data from a single pipe.

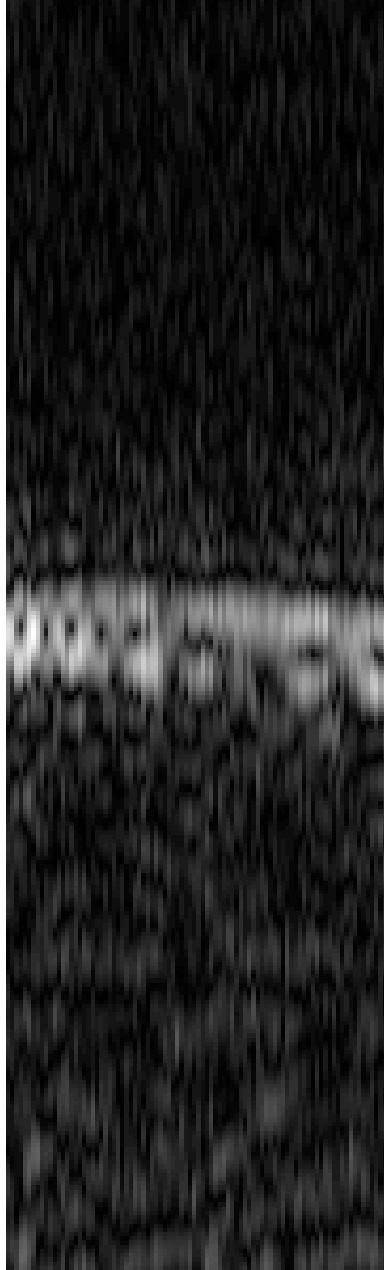


Figure 3.16: Range-angle plot of the (magnitude of) the experimental data from two pipes.

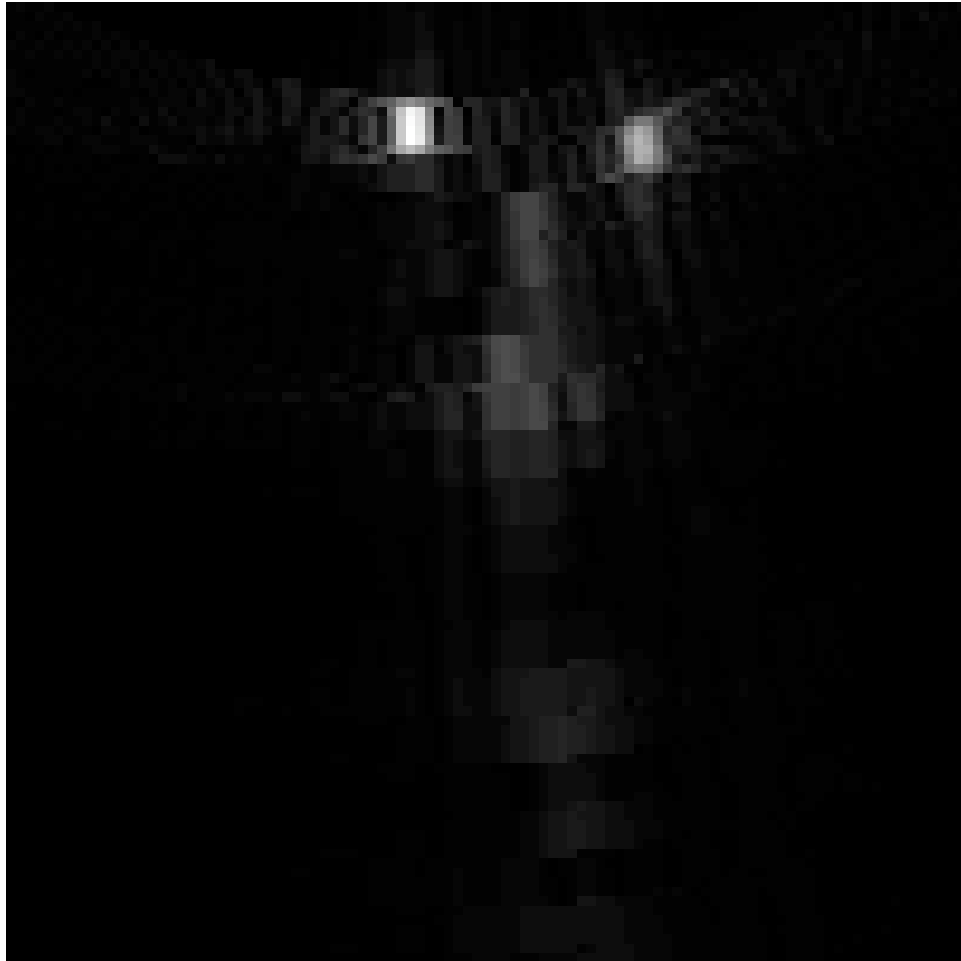


Figure 3.17: The single-bounce backprojected image from the 3-pipe data. The radar moves over  $12^\circ$  at the top.

# Bibliography

- [1] Andersson L-E 1988 On the determination of a function from spherical averages *SIAM J. Math. Anal.* **19** 214–232
- [2] S. Albeverio, F. Gesztesy, and R. Hoegh-Kroem, *Solvable Models in Quantum Mechanics*, Springer, New York, 1988.
- [3] Agranovsky M and Quinto E T 1996 Injectivity sets for the Radon transform over circles and complete systems of radial functions *J. Functional Analysis* **139** 383–414
- [4] Borden B 1999 *Radar imaging of Airborne Targets* (Bristol: Institute of Physics)
- [5] Borden B 2002 Mathematical problems in radar inverse scattering *Inverse Problems* **18** R1–R28
- [6] B. Borden and M. Cheney, "Synthetic-aperture imaging from high-Doppler-resolution measurements", *Inverse Problems* 21 (2005) 1-11.
- [7] Borden B and Cheney M Microlocal ISAR for low signal-to-noise environments *IEEE Trans. on Image Proc.* submitted for review
- [8] Bleistein N, Cohen J K, and Stockwell J W 2000 *The Mathematics of Multidimensional Seismic Inversion* (New York: Springer)
- [9] M. Cheney and R.J. Bonneau, "Imaging that exploits multipath scattering from point scatterers", *Inverse Problems* 20 (2004) 1691-1711
- [10] Chen V C and Ling H 2002 *Time-Frequency Transforms for Radar Imaging and Signal Analysis* (Boston: Artech House)
- [11] Cook C E and Bernfeld M 1967 *Radar Signals* (New York: Academic)
- [12] M. Cheney, "A mathematical tutorial on Synthetic Aperture Radar", *SIAM Review* 43 (2001) 301–312.
- [13] W. C. Carrara, R. G. Goodman, R. M. Majewski, *Spotlight Synthetic Aperture Radar: Signal Processing Algorithms*, Artech House, Boston, 1995.
- [14] J.C. Curlander and R.N. McDonough, *Synthetic Aperture Radar*, Wiley, New York, 1991.

- [15] L.J. Cutrona, “Synthetic Aperture Radar”, in Radar Handbook, second edition, ed. M. Skolnik, McGraw-Hill, New York, 1990.
- [16] J.J. Duistermaat, Fourier Integral Operators, Birkhauser, Boston, 1996.
- [17] A.J. Devaney, “Super-resolution processing of multi-static data using time reversal and MUSIC, to appear, J. Acoust. Soc. Am.
- [18] C. Elachi, Spaceborne Radar Remote Sensing: Applications and Techniques, IEEE Press, New York, 1987.
- [19] G. Franceschetti and R. Lanari, Synthetic Aperture Radar Processing, CRC Press, New York, 1999.
- [20] A. Grigis and J. Sjöstrand, Microlocal Analysis for Differential Operators: An Introduction, London Mathematical Society Lecture Note Series vol. 196, Cambridge University Press, 1994.
- [21] V. Guillemin and S. Sternberg, Geometric Asymptotics, American Math. Society, Providence, 1979.
- [22] Hellsten H and Andersson L-E 1987 An inverse method for the processing of synthetic aperture radar data *Inverse Problems* **3** 111–124
- [23] Herman G T, Tuy H K, Langenberg K J and Sabatier P C 1988 *Basic Methods of Tomography and Inverse Problems* (Philadelphia: Adam Hilger)
- [24] Klemm R 2002 *Principles of space-time adaptive processing* (Cornwall: The Institution of Electrical Engineers)
- [25] Langenberg K J, Brandfass M, Mayer K, Kreutter T, Brüll A, Felinger P and Huo D 1993 Principles of microwave imaging and inverse scattering *EARSeL Adv. Remote Sens.* **2** 163–86
- [26] Louis A and Quinto E T 2000 Local tomographic methods in SONAR *Surveys on Solution Methods for Inverse Problems* ed D Colton, H W Engl, A K Louis, J R McLaughlin and W Rundell (New York: Springer)
- [27] Maass P (1989) Wideband radar: the hyp transform *Inverse Problems* **5** 849–857
- [28] Mensa D L 1981 *High Resolution Radar Imaging* (Dedham, MA: Artech House)
- [29] Natterer F 1986 *The Mathematics of Computerized Tomography* (New York: Wiley)
- [30] Natterer F and Wübbeling F 2001 *Mathematical Methods in Image Reconstruction* (Philadelphia: SIAM)
- [31] R.G. Newton, Scattering of Waves and Particles, Springer, New York, 1982.

- [32] Nilsson S 1997 *Application of fast backprojection techniques for some inverse problems of integral geometry* ( Linköping Studies in Science and Technology, Dissertation No. 499, Linköping University, Sweden)
- [33] Nolan C J and Cheney M 2002 Synthetic aperture inversion *Inverse Problems* **18** 221–36
- [34] C. J. Nolan and W. W. Symes, “Global solution of a linearized inverse problem for the acoustic wave equation”, Comm. in P.D.E., Vol. 22, Nos 5-6, 1997.
- [35] A.V. Oppenheim and R.W. Shafer, Digital Signal Processing, Prentice-Hall, Englewood Cliffs, New Jersey, 1975.
- [36] E.T. Quinto, “Singularities of the X-ray transform and limited data tomography in  $R^2$  and  $R^3$ ”, SIAM J. Math. Anal., 24(1993), 1215-1225.
- [37] Snieder R K and Scales J A 1998 Time-reversed imaging as a diagnostic of wave and particle chaos *Phys. Rev. E* **58** 5668–75
- [38] T.K. Sarkar, M.C. Wicks, M. Salazar-Palma, and R.J. Bonneau, *Smart Antennas*, Wiley, New York, 2003.
- [39] Skolnik M I 1980 *Introduction to Radar Systems* (New York: McGraw-Hill)
- [40] Stutzman W L and Thiele G A 1998 *Antenna Theory and Design*, Second Edition (New York: Wiley)
- [41] Son J S, Thomas G and Flores B C 2001 *Range-Doppler Radar Imaging ad Motion Compensation* (Boston: Artech House)
- [42] Sullivan R J 2000 *Microwave Radar Imaging and Advanced Concepts* (Boston: Artech House)
- [43] F. Trèves, Basic Linear Partial Differential Equations, Academic Press, New York, 1975.
- [44] F. Trèves, Introduction to Pseudodifferential and Fourier Integral Operators, volumes I and II, Plenum Press, New York, 1980.
- [45] Tsang L, Kong J A and Shin R T 1985 *Theory of Microwave Remote Sensing* (New York: Wiley)
- [46] L.J. Ziomek, Underwater Acoustics: A Linear Systems Theory Approach, Academic Press, Orlando, 1985.